

Error boundedness of Correction Procedure via Reconstruction / Flux Reconstruction

Philipp Öffner

December 24, 2019

Abstract

We study the long-time error behavior of correction procedure via reconstruction / flux reconstruction (CPR/FR) methods for linear hyperbolic conservation laws. We show that not only the choice of the numerical flux (upwind or central) affects the growth rate and asymptotic value of the error, but that the selection of bases (Gauß-Lobatto or Gauß-Legendre) is even more important. Using a Gauß-Legendre basis, the error reaches the asymptotic value faster and to a lower value than when using a Gauß-Lobatto basis. Also the differences in the error caused by the numerical flux are not essential for low resolution computations in the Gauß-Legendre case. This behavior is better seen on a particular FR scheme which has a strong connection with the discontinuous Galerkin framework, but holds also for other flux reconstruction schemes with low order resolution computations.

1 Introduction

There exists plenty of examples in the literature where stable approximations of hyperbolic conservation laws exhibit a linear error growth (or nearly linear growth) in time, even though stability of the numerical schemes should guarantee that the solution remains bounded, see [11, 18, 29]. The reason behind this is the following: the error equation for the time variation contains a forcing term generated by the approximation or truncation errors and this forcing term can trigger the unbounded growth of the error.

Simultaneously, there are other examples where the temporal error growth is bounded [1, 23]. Finally, in [27], the author gives an explanation under what conditions the error is or is not bounded in time. The author works with SBP-SAT (Summation-by-Parts/Simultaneous-Approximation-Term) finite difference approximation and deduces that the error behavior depends only on the choice of boundary condition of the problem.

If one considers waves in cavities or with periodic boundary conditions, linear growth is observed as it is investigated in [18], where for inflow-outflow problems one obtains boundedness. In other words, if an appropriate boundary condition (sufficiently dissipative) is applied, the error is bounded. In this framework, the error behavior does not depend on the internal discretization. In [24], the authors analyze the long-time behavior of the error for discontinuous Galerkin spectral element methods (DGSEM). They confirm the conclusion from [27] that the bounded error property is due to the dissipative boundary conditions, but in contrast to [27], in the DGSEM framework the internal approximation has indeed an influence on the behavior of the error. The choice of the numerical flux (upwind or central) is essential for the magnitude of the error and the

speed at which the asymptotic error is reached. With the upwind flux one obtains better results. In this paper, we examine the long-time error behavior for a recent correction procedure via reconstruction (CPR) / flux reconstruction (FR) method. The CPR/FR is a unifying framework for several high-order methods such as discontinuous Galerkin (DG), spectral difference (SD), spectral volume (SV), and the residual distribution methods [2, 21], and includes through special choice of the nodal basis and of the correction matrix the DGSEM of [24]. Here, we investigate not only the numerical flux, but also the selection of nodal basis (Gauß-Legendre and Gauß-Lobatto). We recognize that the selection of the flux function is less important than the choice of the nodal basis for the error behavior. Using Gauß-Legendre basis in the approximation, the error is lower than in the Gauß-Lobatto case and the speed of attaining the error asymptotics is even faster for most of the problems under consideration. The selection of the numerical flux has less influence on the error behavior when using Gauß-Legendre nodes than when applying a Gauß-Lobatto basis. Our investigation leads us to the conclusion that for many problems Gauß-Legendre points are the right choice, especially for low-order resolutions. Our analysis extends and completes the investigation / predictions from [24] to a more general framework.

The paper is organized as follows: in the second section, we repeat the main ideas of the SBP-CPR/FR methods and demonstrate the connection between CPR/FR and the DG framework. Then, in the section 3 we present the model problem under consideration. In the next section 4 we provide some approximation results and repeat the stability analysis of the SBP-CPR/FR methods. Then, we extend the results from [24] to the linearly stable one-parameter family of Vincent [38] and also consider in our investigation Gauß-Legendre nodes in the section 5. These nodes do not contain the boundary values in one element and this yields a further error term in our error equation. We focus on this additional error term and give an interpretation for it. We confirm our theoretical investigation by numerical tests in the section 6 which includes also one example from [24] for comparison. We mention some limitations of our results and finally, we summarize and discuss these limitations. In the appendix, we show the relation between FR and DG and focus on stability conditions for FR methods as described in [38].

2 Correction Procedure via Reconstruction/Flux Reconstruction using Summation-by-Parts Operators

In the first part, we shortly repeat the main idea of CPR/FR methods using Summation-by-parts Operators (SBP). For the rest of this work, we call them FR methods. We follow the introduction and notation given in the articles [35, 36].

We consider a one-dimensional scalar conservation law

$$\partial_t u(x, t) + \partial_x f(u(x, t)) = 0, \quad t > 0, x \in (0, L) \quad (1)$$

equipped with adequate initial and boundary conditions. The domain $(0, L)$ is split into K non-overlapping elements $[0, L] = [x^0, x^1] \cup \dots \cup [x^{K-1}, x^K]$. The FR method is a semidiscretization applying a polynomial approximation on elements. Each interval $[x^{k-1}, x^k]$ is transferred onto a standard element. In our case we consider $[-1, 1]$ and all calculations are conducted within this reference element. The term $\frac{\Delta x_k}{2} = \frac{x^k - x^{k-1}}{2}$ denotes the transformation factor. Let \mathbb{P}^N be the space of polynomials of degree $\leq N$, $-1 \leq \xi_i \leq 1$ ($0 \leq i \leq N$) be the interpolation points in $[-1, 1]$, $\mathbb{I}^N : C([-1, 1]) \rightarrow \mathbb{P}^N[-1, 1]$ the interpolation operator and $P_{N-1}^m u$ the orthogonal projection of u onto \mathbb{P}^{N-1} with respect to the inner product of the Sobolev space $H^m((-1, 1))$. The solution u

is approximated by a polynomial $U \in \mathbb{P}^N$. A nodal Lagrange basis is usually employed¹. Instead of working with U one can also express the numerical solution as the vector \underline{u} with coefficients $\underline{u}_i = U(\xi_i), i \in \{0, \dots, N\}$. All the relevant information are stored in these coefficients and one may write

$$u(\xi) \approx U(\xi) = \sum_{i=0}^N \underline{u}_i l_i(\xi), \quad (2)$$

where $l_i(\xi)$ is the i -th Lagrange interpolation polynomial that satisfies $l_i(\xi_j) = \delta_{ij}$. In finite difference (FD) schemes, it is common to work with the coefficients only and since we are working with SBP operators with origins lying in the FD community [25], we utilize the coefficients as well. The flux $f(u)$ is also approximated by a polynomial, where the coefficients are given by $\underline{f}_i = f(\underline{u}_i) = f(U(\xi_i))$.

With respect to the selected basis (interpolation points), an approximation of the derivative is represented by the matrix \underline{D} . Moreover, a discrete scalar product is represented by the symmetric and positive mass/norm matrix \underline{M} . This matrix approximates the usual \mathbf{L}^2 scalar product. It is

$$\underline{D} \underline{u} \approx \underline{\partial_x u} \text{ and } (\underline{u}, \underline{v})_N := \underline{u}^T \underline{M} \underline{v} \approx \int_{x^{k-1}}^{x^k} uv \, dx. \quad (3)$$

Applying Lagrange polynomials, we obtain $D_{ij} = l'_j(\xi_i)$. The matrix $\underline{M} = \text{diag}(\omega_0, \dots, \omega_N)$ is associated as usual with the quadrature rule given by the polynomial basis (Gauß-Lobatto or Gauß-Legendre) where ω_j are the quadrature weights associated with the nodes ξ_j . For Gauß-Legendre nodes, $\omega_j = \int_{-1}^1 l_j(x) \, dx$. Note that in case of Gauß-Lobatto nodes, the mass matrix is in general not exact. As described in the review articles [12, 37] SBP operators are constructed in such way that they mimic integration-by-parts on a discrete level. Up to now, we have expressions for the derivative as well as for the integration. Hence, the evaluation on the boundary is missing. Here, we have to introduce two different operators. First, the restriction operator denoted by the matrix \underline{R} which approximates the interpolation of a function to the boundary points $\{x^{k-1}, x^k\}$. Second, the diagonal boundary matrix $\underline{B} = \text{diag}(-1, 1)$ that gives the difference of boundary values. This means

$$\underline{R} \underline{u} \approx \begin{pmatrix} u(x^{k-1}) \\ u(x^k) \end{pmatrix} \text{ and } (u_L, u_R) \underline{B} \begin{pmatrix} v_L \\ v_R \end{pmatrix} = u_R v_R - u_L v_L.$$

where v_i ($i = L, R$) describes the position in the element, i.e. the left and right boundary points. Finally, all operators are introduced and they have to fulfill the SBP property

$$\underline{M} \underline{D} + \underline{D}^T \underline{M} = \underline{R}^T \underline{B} \underline{R}, \quad (4)$$

in order to mimic integration-by-parts on a discrete level

$$\underline{u}^T \underline{M} \underline{D} \underline{v} + \underline{u}^T \underline{D}^T \underline{M} \underline{v} \approx \int_{x^{k-1}}^{x^k} u (\partial_x v) \, dx + \int_{x^{k-1}}^{x^k} (\partial_x u) v \, dx = uv \Big|_{x^{k-1}}^{x^k} \approx \underline{u}^T \underline{R}^T \underline{B} \underline{R} \underline{v}. \quad (5)$$

As an example, we consider Gauss-Lobatto nodes in $[-1, 1,]$ which include the boundary points. Then, the restriction operators are simply

$$\underline{R} = \begin{pmatrix} 1 & 0 & \dots & 0 & 0 \\ 0 & 0 & \dots & 0 & 1 \end{pmatrix}, \quad \underline{R}^T \underline{B} \underline{R} = \text{diag}(-1, 0, \dots, 0, 1). \quad (6)$$

The general aspects of SBP operators are introduced and we focus on our FR approach now. Contrary to DG methods, we do not use a variational formulation (i.e. weak form) of (1). Instead,

¹Modal bases are also possible [36], but we won't consider these in this paper.

the differential form is applied, corresponding to a strong form DG method. To describe the semidiscretisation all operators are introduced. We apply the discrete derivative matrix \underline{D} to \underline{f} . The divergence is $\underline{D}\underline{f}$. Since the numerical solutions will probably have discontinuities across elements, we will have this in the discrete flux, too. In order to avoid this problem, a numerical flux f^{num} is introduced which computes a common flux at the boundary using values from both neighboring elements. The main idea of the FR schemes is that the numerical flux at the boundaries will be corrected by functions in such manner that information of two neighboring elements interact and basic properties, like conservation, hold also in the semidiscretisation. Therefore, we add a correction term using a correction matrix \underline{C} at the boundary nodes. This gives *Flux Reconstruction* its name. Hence, a simple FR method for (1) reads

$$\partial_t \underline{u} = -\underline{D}\underline{f} - \underline{C} \left(f^{\text{num}} - \underline{R}\underline{f} \right). \quad (7)$$

A general choice of the correction matrix \underline{C} recovers the linearly stable flux reconstruction methods of [38, 39], as presented in [35].

In our investigation, we only consider the one parameter² family of Vincent et al. [38]. To describe the setting and to specify the correction matrix, we introduce a symmetric matrix $\tilde{\underline{K}}$ satisfying $\underline{M} + \tilde{\underline{K}} > 0$, i.e. positive definite. Then, the correction matrix $\underline{C} = (\underline{M} + \tilde{\underline{K}})^{-1} \underline{R}^T \underline{B}$ is applied in (7) where $\tilde{\underline{K}}$ is defined through:

$$\tilde{\underline{K}} = \kappa (\underline{D}^N)^T \underline{M} \underline{D}^N, \quad \text{with } \tilde{\underline{K}} \underline{D} = 0. \quad (8)$$

The term κ represents the free parameter and the selection of κ yields different numerical methods. In particular, $\kappa \equiv 0$ is the canonical choice of the correction matrix and the resulting scheme corresponds to a strong form of a DG method [14]. Furthermore, since (8) holds ($\underline{D}^{N+1} = 0$ (polynomials of degree $\leq N$)) and $\tilde{\underline{K}}$ is symmetric, we may write

$$\left(\underline{M} + \tilde{\underline{K}} \right) \underline{D} + \underline{D}^T \left(\underline{M} + \tilde{\underline{K}} \right) \stackrel{(8)}{=} \underline{M} \underline{D} + \underline{D}^T \underline{M} \stackrel{(4)}{=} \underline{R}^T \underline{B} \underline{R}. \quad (9)$$

Therefore, the SBP property is also valid for $\underline{M} + \tilde{\underline{K}}$.

Remark 2.1. The only condition on κ is given by the requirement that $\underline{M} + \tilde{\underline{K}}$ is positive definite. It is essential since the term represents a norm in the discrete setting and linear stability will be analyzed in respect to this discrete norm in subsection 4.2. To guarantee that the term $\underline{M} + \tilde{\underline{K}}$ with (8) is positive definite, κ has to be bounded from below. In [35, Section 3.6], the bounds on κ are determined and we repeat them here for completeness. The superscript denotes the used nodes (Gauß-Legendre with G , Gauß-Lobatto with L). With $a_N = \frac{(2N)!}{2^N (N!)^2}$, we get the following bounds:

$$\kappa > \kappa_-^G := -\frac{1}{(2N+1)a_N^2(N!)^2}, \quad \kappa > \kappa_-^L := -\frac{1}{Na_N^2(N!)^2}$$

Furthermore, we like to mention that the investigation is based on an idea of Jameson [22]. Instead of working with the classical \mathbf{L}^2 norm, he applies a broken Sobolev norm involving derivatives and the argument that in finite-dimensional vector spaces all norms are equivalent. In the appendix 8, we give the definition of the used norm together with more explanations and an example about the connection between DG methods and the FR framework.

As we already mentioned before, the different selection of κ yields various numerical methods. In

²The results for the multi-parameter family are similar to those about the one parameter family, since the one parameter family is contained in the extended range of schemes. the one parameter family for simplicity.

N	κ_{SD}	κ_{Hu}	κ_{DG}
2	4/135	1/15	0
3	1/1050	8/4725	0
4	8/496125	1/39690	0
5	1/5893965	12/49116375	0

Table 1: Values of κ to get different numerical schemes [38]

table 1, we provide the terms κ for, in our opinion, the most popular FR schemes for different order of accuracy. The exact formulas can be found in the appendix.

Theoretically, the parameter κ can tend to infinity as it is described and analyzed in the same paper. However, the numerical results in [35, 38] show that the most accurate results are obtained when $\kappa = 0$ is used and significant accuracy is lost for $\kappa \rightarrow \infty$. Hence, we restrict ourself in the investigation and consider schemes between the range of DG, spectral difference and Huynh scheme [20]. We assume the following:

Asumption 2.2. With increased N , κ tends to zero. It is $\kappa \in \mathcal{O}(N^{-1}(a_N N!)^{-2})$.

3 Model Problem

To analyze the long time error behavior of SBP-FR method, we study (similarly to [24, 27]) the scalar linear advection equation with non-periodic boundary conditions

$$\begin{aligned} \partial_t u + \partial_x u &= 0, & x \in [0, L], & t \geq 0 \\ u(t, 0) &= g(t), \\ u(0, x) &= u_0(x). \end{aligned} \tag{10}$$

We assume also that the initial and boundary values are chosen in such way that $u(t, \cdot) \in H_{\kappa, N}^m((0, L))$ for $m > 1$ and that $\|u(t, \cdot)\|_{H_{\kappa, N}^m}$ is uniformly bounded in time. As it is described in [24], such conditions are physically meaningful, because they describe problems where the boundary input is, for instance, sinusoidal. In our numerical tests in section 6, we will present an example where these conditions are not fulfilled, see subsection 6.2. Here, $H_{\kappa, N}^m$ denotes the following function space

$$H_{\kappa, N}^m((0, L)) = \{u \in \mathbf{L}^2((0, L)) \mid \forall |j| \leq m : u^{(j+N)} \in \mathbf{L}^2((0, L))\}$$

equipped with the norm

$$\|u\|_{H_{\kappa, N}^m} := \left(\sum_{j=0}^m \|u^{(j)}\|_{\mathbf{L}^2((0, L))}^2 + \kappa \|u^{(j+N)}\|_{\mathbf{L}^2((0, L))}^2 \right)^{\frac{1}{2}}. \tag{11}$$

In total, the highest derivative is $m + N$. If N tends to infinity, κ tends to zero rapidly because of our assumption 2.2. This means nothing else that in (11), the first term is always dominant in the norm calculation³. We will use this fact later in the estimation of the error. As it is well-known, the boundary conditions of (10) have an essential impact on the solution and in [28], the author also shows that a correct implementation of the boundary conditions is essential for well-posedness.

³Instead of working with $H_{\kappa, N}^m$ we also may work directly H^{m+N} in our investigation since we always assume sufficient smoothness of the solution.

We shortly give the following example from [24] in the DG context whereas for general FR schemes the analysis can be found in [38, 39].

Example 3.1. Here, the energy of the solution u of the initial boundary value problem (10) is measured by the standard \mathbf{L}^2 -norm $\|u\|^2 = \int_0^L u^2 dx$. Focusing on the weak formulation of the advection equation (10), we multiply with a test function $\varphi \in C^1([0, L])$ and integrate over the domain. We get

$$\int_0^L u_t \varphi dx + \int_0^L u_x \varphi dx = 0.$$

Taking $\varphi = u$ and integration by parts yield

$$\frac{1}{2} \frac{d}{dt} \|u\|^2 = -\frac{1}{2} \int_0^L uu_x dx = \frac{1}{2} \left(g^2(t) - u^2(L, t) \right).$$

Integration in time over an interval $[0, T]$ leads to

$$\|u(T)\|^2 + \int_0^T u^2(L, t) dt = \|u_0\|^2 + \int_0^T g^2(t) dt. \quad (12)$$

We see that the energy at time T can be expressed by the initial energy plus the energy added at the left side through the boundary condition minus the energy, which we lose through the right side. Therefore, the selection of the boundary conditions is essential and the numerical approximation has to imitate this.

4 Approximation Results and Stability of the SBP-FR Methods

4.1 Numerical Errors and Approximation Results

Before we start with our stability analysis of the SBP-FR methods and derive the error equations in the next section 5, we give an overview of the notation and some basic approximation properties which will be used later in this paper. In table 2, we summarize the applied notation for clarification. We analyze stability in the semidiscrete sense. Therefore, we divide the entire interval $[0, L]$ into elements $e^k = [x^{k-1}, x^k]$, $k = 1, \dots, K$, where the x^k are the element boundaries, and in particular where $x^0 = 0$ and $x^K = L$. As it was explained in section 2, we transform every element to our standard element and use a SBP-FR method. We investigate both Gauß-Lobatto and Gauß-Legendre quadrature. We can define the discrete inner product by

$$(U, V)_N := \sum_{j=0}^N U(\xi_j) V(\xi_j) \omega_j. \quad (13)$$

For Gauß-Lobatto ($UV \in \mathbb{P}^{2N-1}$) / Gauß-Legendre ($UV \in \mathbb{P}^{2N+1}$) quadrature, it holds

$$(U, V)_N = \sum_{j=0}^N U(\xi_j) V(\xi_j) \omega_j = \int_{-1}^1 UV d\xi \quad \forall UV \in \mathbb{P}^{2N-1} / \mathbb{P}^{2N+1}.$$

We choose the numerical flux to have the form

$$f^{\text{num}}(U_L, U_R) = \frac{U_L + U_R}{2} - \frac{\sigma}{2} (U_R - U_L), \quad \sigma \in [0, 1],$$

where U_L, U_R are the states on the left and right. For $\sigma = 0$ we get the central flux and for $\sigma = 1$ the upwind flux is obtained. At the physical boundaries we apply always the upwind flux

together with g at the left boundary and the calculated value at the right boundary. We analyze the temporal behavior of the error which is given by $E^k := u^k(x(\xi), t) - U^k(\xi, t)$. We denote by u^k the restriction of u on the k -th interval and term $x(\xi)$ denotes the transformation from the point ξ in the reference interval to point x in the k -th interval. We can split the error into two parts:

$$E^k = \underbrace{(\mathbb{I}^N(u^k) - U^k)}_{=:\varepsilon_1^k \in \mathbb{P}^N} + \underbrace{(u - \mathbb{I}^N(u^k))}_{=:\varepsilon_p^k}. \quad (14)$$

We will investigate discrete norms in this context using the discrete inner products (13). The global norm, which depends only on t , is defined by

$$\|U(t)\|_N^2 := \sum_{k=1}^K \frac{\Delta x_k}{2} \|U^k(t)\|_N^2 = \sum_{k=1}^K \frac{\Delta x_k}{2} \underline{u}^{k,T} \underline{M} \underline{u}^k, \quad (15)$$

and $U(0)$ is the interpolant of the initial condition u_0 . In (15) we provide for the norm both the notation with the coefficients and with the polynomial solution. They are identical. With the triangle inequality, we can bound the error (14) by

$$\|E^k\|_N \leq \|\varepsilon_1^k\|_N + \|\varepsilon_p^k\|_N. \quad (16)$$

The form ε_p^k is the interpolation error, which is the sum of the series truncation error and of the aliasing error. As it was already described in [6, 13, 16, 17, 30, 32], the continuous norms converge spectrally fast for the different bases under consideration if $u \in C^\infty((-1, 1))$. We denote by

$$|u|_{H^{m;N}((-1,1))} := \left(\sum_{j=\min(m, N+1)}^m \|u^{(j)}\|_{\mathbf{L}^2((-1,1))}^2 \right)^{\frac{1}{2}}$$

the semi-norms of the Sobolev space $H^m((-1, 1))$, by P_N the projection operator of the truncated Legendre series ⁴ and by \mathbb{I}^N the interpolation operator from section 2. We get:

- Gauß-Lobatto/Gauß-Legendre points

$$\|u - \mathbb{I}^N(u)\|_{\mathbf{L}^2((-1,1))} \leq CN^{-m} |u|_{H^{m;N}((-1,1))}; \quad (17)$$

where C depends on m . The generalization of these formulas (17) and (20) for $1 \leq l \leq m$ are

- Gauß-Lobatto/Gauß-Legendre points

$$\|u - \mathbb{I}^N(u)\|_{H^l((-1,1))} \leq CN^{2l-\frac{1}{2}-m} |u|_{H^{m;N}((-1,1))}; \quad (18)$$

In view of our investigation, we need to consider our interpolation error not only in the standard interval $[-1, 1]$, but in each element e^k . Therefore, we will transform our estimations (17),(20) to every element. We get with the interval length $\Delta x^k = x^k - x^{k-1}$:

- Gauß-Lobatto/Gauß-Legendre⁵ points (Combination of [13, Theorem 6.6.1] and [6, Section 5.4.4])

$$\|\varepsilon_p^k\|_{H^n(e^k)} \leq C \left(\Delta x^k \right)^{n-\min\{m, N\}+\frac{1}{2}} N^{n-m+\frac{1}{2}} |u|_{H^{m;N}(e^k)}; \quad (19)$$

for $n = 0, 1$. For Gauß-Lobatto, the exponents in (19) are reduced by $\frac{1}{2}$.

⁴See section 5.4.2 of [6] for detail.

⁵ A more a detailed analysis can be found in [4, 5].

We have introduced all the needed approximation estimations.

Remark 4.1. We want to point out that the following investigation can also be done using a modal Legendre basis. Here, we would assume exact integration and the matrix \underline{M} would also be diagonal, see [36] for details. Hence, the interpolation operator in the equation (14) can be replaced by the projection operator and the *interpolation error* is only the series truncation error. The analysis for a modal Legendre basis is similar to the Gauß-Legendre case and can be transferred with equivalent estimations to (17)-(19) for the projection operator. For example, instead of (17) we apply

$$\|u - P_N(u)\|_{\mathbf{L}^2((-1,1))} \leq CN^{-m} |u|_{H^{m;N}((-1,1))}. \quad (20)$$

4.2 Stability of the SBP-FR Methods

We follow the steps from [24] and start by repeating the main aspects of the stability analysis of the SBP-FR methods, see [35] for details. Then, we derive an error equation for the SBP-FR methods for the model problem (10) in the following section 5. In [24] the authors investigate the long-time error behavior for the Discontinuous-Galerkin-Spectral-Element Method (DGSEM) using Gauß-Lobatto nodes. Here, we make two extensions to their investigation. First, we also consider Gauß-Legendre nodes and secondly, we also investigate the long-time error behavior of the one-parameter family of Vincent et al. where the DGSEM is included.

Instead of using the discrete norm which is represented by \underline{M} and corresponds to the continuous \mathbf{L}^2 -norm we are applying $\underline{M} + \tilde{\mathbf{K}}$ analogously to [35] and introduced in section 2. We are studying the change of the discrete norm

$$\|\underline{u}^k\|_{M+\tilde{K}}^2 = (\underline{u}^k, \underline{u}^k)_{M+\tilde{K}} = \underline{u}^{k,T} (\underline{M} + \tilde{\mathbf{K}}) \underline{u}^k \quad (21)$$

for the total energy. We multiply $\underline{\varphi}^{k,T} (\underline{M} + \tilde{\mathbf{K}})$ to equation (7). Here, the term k describes the element and T means only the transposed vector. We get

$$\frac{\Delta x_k}{2} \underline{\varphi}^{k,T} (\underline{M} + \tilde{\mathbf{K}}) \partial_t \underline{u}^k = -\underline{\varphi}^{k,T} (\underline{M} + \tilde{\mathbf{K}}) \underline{D} \underline{u}^k - \underline{\varphi}^{k,T} (\underline{M} + \tilde{\mathbf{K}}) \underline{C} (\underline{f}^{\text{num},k} - \underline{R} \underline{u}^k). \quad (22)$$

With $\underline{\varphi}^k = \underline{u}^k$ and $\underline{C} = (\underline{M} + \tilde{\mathbf{K}})^{-1} \underline{R}^T \underline{B}$ it comes:

$$\frac{\Delta x_k}{2} \underline{u}^{k,T} (\underline{M} + \tilde{\mathbf{K}}) \partial_t \underline{u}^k = -\underline{u}^{k,T} (\underline{M} + \tilde{\mathbf{K}}) \underline{D} \underline{u}^k - \underline{u}^{k,T} \underline{R}^T \underline{B} (\underline{f}^{\text{num},k} - \underline{R} \underline{u}^k), \quad (23)$$

where the numerical flux is given by $\underline{f}^{\text{num},k} = (f_L^{\text{num},k}, f_R^{\text{num},k})^T$. With $\tilde{\mathbf{K}} \underline{D} = 0$ and the SBP property (9), the above equation (23) can be written as

$$\frac{\Delta x_k}{2} \underline{u}^{k,T} (\underline{M} + \tilde{\mathbf{K}}) \partial_t \underline{u}^k = \underline{u}^{k,T} \underline{D}^T \underline{M} \underline{u}^k - \underline{u}^{k,T} \underline{R}^T \underline{B} \underline{R} \underline{u}^k - \underline{u}^{k,T} \underline{R}^T \underline{B} (\underline{f}^{\text{num},k} - \underline{R} \underline{u}^k). \quad (24)$$

Adding (23) with (24), using the symmetry of the scalar product induced by \underline{M} and dividing by two yields

$$\frac{\Delta x_k}{4} \frac{d}{dt} \|\underline{u}^k\|_{M+\tilde{K}}^2 = -\underline{u}^{k,T} \underline{R}^T \underline{B} (\underline{f}^{\text{num},k} - \underline{R} \underline{u}^k) - \frac{1}{2} \underline{u}^{k,T} \underline{R}^T \underline{B} \underline{R} \underline{u}^k. \quad (25)$$

The rate of change of the total energy is the sum over all elements.

$$\frac{1}{2} \frac{d}{dt} \sum_{k=1}^K \frac{\Delta x_k}{2} \|\underline{u}^k\|_{M+\tilde{K}}^2 = - \sum_{k=1}^K \underline{u}^{k,T} \underline{R}^T \underline{B} (\underline{f}^{\text{num},k} - \frac{1}{2} \underline{R} \underline{u}^k). \quad (26)$$

If we now split the sum into three parts and use the fact that the numerical flux is unique at the interface of two elements, we can rewrite⁶ (26) as

$$\begin{aligned} \frac{1}{2} \frac{d}{dt} \sum_{k=1}^K \frac{\Delta x_k}{2} \|u^k\|_{M+\tilde{K}}^2 &= \frac{1}{2} \frac{d}{dt} \sum_{k=1}^K \frac{\Delta x_k}{2} \|U^k(t)\|_{M+\tilde{K}}^2 = - \sum_{k=1}^K u^{k,T} \underline{R}^T \underline{B} \left(f^{\text{num},k} - \frac{1}{2} \underline{R} u^k \right) \\ &= \frac{1}{2} g(t)^2 - \frac{1}{2} \left(U_L^1(t) - g(t) \right)^2 - \frac{1}{2} \left(U_R^K(t) \right)^2 - \frac{\sigma}{2} \sum_{k=2}^K \left(\llbracket U^k(t) \rrbracket \right)^2, \end{aligned}$$

where U_i ($i = L, R$) describe the approximated solution (2) and where the indices give the position in the elements. The term $\llbracket U^k \rrbracket := U_R^{k-1} - U_L^k$ is the jump. We define the global norm corresponding to $\underline{M} + \tilde{\underline{K}}$ by $\|U(t)\|_{\tilde{\underline{K}}_M}^2 := \sum_{k=1}^K \frac{\Delta x_k}{2} \|U^k(t)\|_{M+\tilde{K}}^2$ and set $U(0)$ the interpolant of the initial condition u_0 . The integration from zero to T yields

$$\|U(T)\|_{\tilde{\underline{K}}_M}^2 + \int_0^T \left(U_R^K(t) \right)^2 dt + \int_0^T \left(U_L^1(t) - g(t) \right)^2 dt + \sigma \int_0^T \sum_{k=2}^K \left(\llbracket U^k \rrbracket \right)^2 dt = \|U(0)\|_{\tilde{\underline{K}}_M}^2 + \int_0^T g^2(t) dt,$$

which also satisfies

$$\|U(T)\|_{\tilde{\underline{K}}_M}^2 + \int_0^T \left(U_R^K(t) \right)^2 dt \leq \|U(0)\|_{\tilde{\underline{K}}_M}^2 + \int_0^T g^2(t) dt. \quad (27)$$

This has already been proven more generally in [35, Theorem 5]. Let us mention that the norms under consideration are fully discrete. However, the same schemes are analyzed as described in [38]. Before starting with the analysis in the next section 5, we shortly repeat again the notation which will be used in this paper in table 2 for clarification, and we also repeat the assumptions which are made. We introduce some abbreviations which are used in the next section.

5 Long-time Error Behavior for SBP-FR

The error is investigate in respect to the global discrete norm $\|\cdot\|_{\tilde{\underline{K}}_M}$. It is given by $E^k = u^k(x(\xi), t) - U^k(\xi, t)$ within any element. Using (14) and the triangle inequality, we can bound the error by

$$\|E^k\|_{M+\tilde{K}} \leq \|\varepsilon_1^k\|_{M+\tilde{K}} + \|\varepsilon_p^k\|_{M+\tilde{K}}. \quad (28)$$

Instead of focusing on both terms in (28), we derive the error equation only for ε_1^k since this term has the major influence on the error behaviors. First, ε_p^k is simply an interpolation error of the exact solution, and so there is actually no process / mechanism in the procedure which might lead to any accumulation of the ε_p^k errors.

Secondly, by following the ideas / steps of [24], we do not further consider the terms ε_p^k due to the following fact. We are working in a finite dimensional normed vector space. All norms are equivalent in this vector space and this allows us to bound the discrete norm

$$\|\varepsilon_p^k\|_{M+\tilde{K}}^2 = (\varepsilon_p^k, \varepsilon_p^k)_{M+\tilde{K}} = \varepsilon_p^{k,T} (\underline{M} + \tilde{\underline{K}}) \varepsilon_p^k \stackrel{(8)}{=} \varepsilon_p^{k,T} \underline{M} \varepsilon_p^k + \varepsilon_p^{k,T} \kappa(\underline{D}^N)^T \underline{M} \underline{D}^N \varepsilon_p^k \quad (29)$$

⁶Details can be found in [24, 35] as well as in section 5.

<i>Notation</i>	<i>Interpretation / Assumptions</i>
u	is the solution of (10). It is $u \in H_{\kappa,N}^m$.
U	is the spatial approximation of u given by (2). It is $U \in \mathbb{P}^N$.
\underline{u}	are the coefficients of U , evaluated at the interpolation / quadrature nodes.
\underline{D}	is the discrete derivative matrix.
\underline{R}	is the restriction operator performing interpolation to the boundary.
\underline{M}	is the diagonal mass / norm matrix.
\underline{K}	is a symmetric matrix to build different FR schemes. It is defined in (8).
κ	Free parameter to define the different FR schemes from (8), bounded from below and tends to zero for increasing polynomial order N .
$\langle \cdot, \cdot \rangle$	is the usual \mathbf{L}^2 scalar product.
$\ \cdot \ $	is the norm induced by the \mathbf{L}^2 scalar product.
$(\cdot, \cdot)_N$	is the discrete scalar product given by (13).
$\ \cdot \ _N$	is the norm induced by the discrete scalar product from above.
$\ \cdot \ _{M+\bar{K}}$	is the norm (21) induced by the discrete scalar product with respect to $\underline{M} + \underline{K}$.
$\ \cdot \ _{\bar{K}_M}$	is global norm corresponding to $\underline{M} + \underline{K}$.
\mathbb{I}^N	is the interpolation operator.
$P_{N-1}^m(u)$	is the orthogonal projection of u onto $\mathbb{P}^{N-1}((-1, 1))$ using the inner product of $H^m((-1, 1))$.
$E^k = u^k - U^k$	is the total error in the k -th element.
$\varepsilon_1^k := \mathbb{I}^N(u^k) - U^k$	is the difference between interpolation and spatial approximation in the k -th element.
$\varepsilon_p^k = u^k - \mathbb{I}^N(u^k)$	is the interpolation error.

Table 2: Summary of the notations used in this article.

in terms of the continuous ones from the Sobolev space H^m . Since u is sufficiently smooth (i.e. $u \in H_{\kappa,N}^m$ with $m > 1$), the continuous norms can be estimated by (17) - (19) and we obtain a spectral decay for the interpolation error ε_p^k . In other words, we have to investigate the error behavior of ε_1^k in detail. Here, we follow the approach from [24]. Before we derive the error equation for ε_1^k , we give the main result along with a short description of the main steps of the analysis

Result 5.1. The factor $\eta(t)$ given in (44) depends on ε_1 . If the mean of η can be bounded from below by a positive constant δ_0 , i.e. $\bar{\eta} \geq \delta_0 > 0$, then there exists a constant C_1 such that the errors $\varepsilon_1^k(t)$ of (28) satisfies the inequality

$$\|\varepsilon_1(t)\|_{\bar{K}_M} \leq \frac{1 - \exp(-\delta_0 t)}{\delta_0} C_1 \quad (30)$$

in the discrete norm $\| \cdot \|_{\bar{K}_M}$. The total error is bounded in time.

In the following, the exact conditions for the above inequality to be fulfilled will be derived and we specify in detail what factors play a key role in the definition of η and δ_0 . We outline the major steps of our analysis:

1. Inserting the error E^k into the continuous equation in every element leads us to an error equation for ε_1^k .

2. Adding zero in a suitable way gives us the possibility to split the equations into a continuous and a discrete part.
3. We add both parts for every element and obtain the error behavior for the total domain.
4. By estimating the continuous terms we get an inequality for the error ε_1 in the discrete norms and with some assumptions we retrieve the long-time error behavior of ε_1 .

We derive now the error equation for $\varepsilon_1^k = \mathbb{I}^N(u^k) - U^k$.

We are searching the solution u of the continuous equation

$$\frac{\Delta x}{2} \langle \partial_t u, \varphi^k \rangle + u \varphi \Big|_{-1}^1 - \langle u, \partial_\xi \varphi^k \rangle = 0, \quad (31)$$

where $\langle u, \varphi^k \rangle := \int_{-1}^1 u \varphi^k \, d\xi$ defines the inner product. The equation (31) can be derived from the advection equation (10) by multiplying with the test function φ , integrating over the standard element and using integration-by-parts. With $\varphi^k \in \mathbb{P}^N \subset \mathbf{L}^2$ and $u^k = \mathbb{I}^N(u^k) + \varepsilon_p^k$, we get for the continuous equation

$$\frac{\Delta x_k}{2} \langle \partial_t \mathbb{I}^N(u^k), \varphi^k \rangle + \mathbb{I}^N(u^k) \varphi^k \Big|_{-1}^1 - \langle \mathbb{I}^N(u^k), \partial_\xi \varphi^k \rangle = -\frac{\Delta x_k}{2} \langle \partial_t \varepsilon_p^k, \varphi^k \rangle - \varepsilon_p^k \varphi^k \Big|_{-1}^1 + \langle \varepsilon_p^k, \partial_\xi \varphi^k \rangle. \quad (32)$$

Remark 5.2. For Gauß-Lobatto nodes it holds $\varepsilon_p^k = 0$ at the endpoints because the interpolant is equal to the solution there. Thus, $\varepsilon_p^k \varphi^k \Big|_{-1}^1 = 0$.

Using integration-by-parts for $\langle \varepsilon_p^k, \partial_\xi \varphi^k \rangle$ yields

$$\frac{\Delta x_k}{2} \langle \partial_t \mathbb{I}^N(u^k), \varphi^k \rangle + \mathbb{I}^N(u^k) \varphi^k \Big|_{-1}^1 - \langle \mathbb{I}^N(u^k), \partial_\xi \varphi^k \rangle = -\frac{\Delta x_k}{2} \langle \partial_t \varepsilon_p^k, \varphi^k \rangle - \langle \partial_\xi (\varepsilon_p^k), \varphi^k \rangle. \quad (33)$$

Applying now interpolation, the discrete norm gives for the first term

$$\langle \partial_t \mathbb{I}^N(u^k), \varphi^k \rangle = \left(\partial_t \underline{\mathbb{I}^N(u^k)}, \underline{\varphi^k} \right)_{M+\bar{K}} + \left\{ \langle \partial_t \mathbb{I}^N(u^k), \varphi^k \rangle - \left(\partial_t \underline{\mathbb{I}^N(u^k)}, \underline{\varphi^k} \right)_{M+\bar{K}} \right\}. \quad (34)$$

Since $\varphi^k \in \mathbb{P}^N$ and the exactness of the quadrature formulas, we obtain for the volume term in (33)

$$\langle \mathbb{I}^N(u^k), \partial_\xi \varphi^k \rangle = \left(\underline{\mathbb{I}^N(u^k)}, \partial_\xi \underline{\varphi^k} \right)_N. \quad (35)$$

Finally, the values of the interpolation polynomial at the boundaries of the element (-1 and 1) can be approximated by a limitation process from the left side $\mathbb{I}^N(u^k)^-$ and right side $\mathbb{I}^N(u^k)^+$. To simplify the notation we define

$$\underline{f}^{\text{num},k} \left(\mathbb{I}^N(u^k)^-, \mathbb{I}^N(u^k)^+ \right) := \left(f^{\text{num}} \left(\underline{\mathbb{I}^N_R(u)^{k-1}}, \underline{\mathbb{I}^N_L(u)^k} \right), f^{\text{num}} \left(\underline{\mathbb{I}^N_R(u)^k}, \underline{\mathbb{I}^N_L(u)^{k+1}} \right) \right)^T. \quad (36)$$

We obtain for the approximation

$$\begin{aligned} \mathbb{I}^N(u^k) \varphi^k \Big|_{-1}^1 &= \underline{\varphi}^{T,k} \underline{R}^T \underline{B} \underline{f}^{\text{num},k} \left(\mathbb{I}^N(u^k)^-, \mathbb{I}^N(u^k)^+ \right) \\ &\quad + \left(\varphi^k \mathbb{I}^N(u^k) \Big|_{-1}^1 - \underline{\varphi}^{T,k} \underline{R}^T \underline{B} \underline{f}^{\text{num},k} \left(\mathbb{I}^N(u^k)^-, \mathbb{I}^N(u^k)^+ \right) \right). \end{aligned}$$

u is continuous ($m > 1$). Using Gauß-Lobatto points the error term in the braces is zero, because the interpolation polynomial is evaluated at these boundaries and the numerical flux is unique. For Gauss-Legendre points, we get an additional error term which corresponds to an interpolation error (in the pointwise sense) at these end points. The numerical flux is again unique and so the error term reads

$$\varepsilon_{2,\varphi}^k := \left(\varphi^k \mathbb{I}^N(u^k) \Big|_{-1}^1 - \underline{\varphi}^{T,k} \underline{\mathbf{R}}^T \underline{\mathbf{B}} \underline{\mathbf{f}}^{\text{num},k} \left(\mathbb{I}^N(u^k)^-, \mathbb{I}^N(u^k)^+ \right) \right) \quad (37)$$

in the k -th element. Finally, using (35)-(37) in (34) we obtain

$$\begin{aligned} & \frac{\Delta x_k}{2} \left(\partial_t \mathbb{I}^N(u^k), \underline{\varphi}^k \right)_{M+\tilde{\mathbf{K}}} + \underline{\varphi}^{T,k} \underline{\mathbf{R}}^T \underline{\mathbf{B}} \underline{\mathbf{f}}^{\text{num},k} \left(\mathbb{I}^N(u^k)^-, \mathbb{I}^N(u^k)^+ \right) - \left(\mathbb{I}^N(u^k), \partial_\xi \underline{\varphi}^k \right)_{M+\tilde{\mathbf{K}}} \\ &= - \frac{\Delta x_k}{2} \left\langle \partial_t \varepsilon_p^k, \varphi^k \right\rangle - \left\langle \partial_\xi(\varepsilon_p^k), \varphi^k \right\rangle - \frac{\Delta x_k}{2} \left\{ \left\langle \partial_t \mathbb{I}^N(u^k), \varphi^k \right\rangle - \left(\partial_t \mathbb{I}^N(u^k), \underline{\varphi}^k \right)_{M+\tilde{\mathbf{K}}} \right\} - \varepsilon_{2,\varphi}^k. \end{aligned} \quad (38)$$

Adding zero to the terms in the curly braces and using

$$\begin{aligned} \left\langle \partial_t \mathbb{I}^N(u^k), \varphi^k \right\rangle - \left(\partial_t \mathbb{I}^N(u^k), \underline{\varphi}^k \right)_{M+\tilde{\mathbf{K}}} &= \left\langle \underbrace{\partial_t \left(\mathbb{I}^N(u^k) - P_{N-1}^m \left(\mathbb{I}^N(u^k) \right) \right)}_{=: Q(u^k)}, \varphi^k \right\rangle \\ &\quad - \left(\partial_t \left(\mathbb{I}^N(u^k) - P_{N-1}^m \left(\mathbb{I}^N(u^k) \right) \right), \underline{\varphi}^k \right)_{M+\tilde{\mathbf{K}}}, \end{aligned}$$

with P_{N-1}^m the orthogonal projection operator⁷ of u onto \mathbb{P}^{N-1} yields in (38)

$$\begin{aligned} & \frac{\Delta x_k}{2} \left(\partial_t \mathbb{I}^N(u^k), \underline{\varphi}^k \right)_{M+\tilde{\mathbf{K}}} + \underline{\varphi}^{T,k} \underline{\mathbf{R}}^T \underline{\mathbf{B}} \underline{\mathbf{f}}^{\text{num},k} \left(\mathbb{I}^N(u^k)^-, \mathbb{I}^N(u^k)^+ \right) - \left(\mathbb{I}^N(u^k), \partial_\xi \underline{\varphi}^k \right)_{M+\tilde{\mathbf{K}}} \\ &= \frac{\Delta x_k}{2} \left\langle T^k(u), \varphi^k \right\rangle + \frac{\Delta x_k}{2} \left(Q(u^k), \underline{\varphi}^k \right)_{M+\tilde{\mathbf{K}}} - \varepsilon_{2,\varphi}^k, \end{aligned} \quad (39)$$

where $T^k(u) = - \left\{ \partial_t \varepsilon_p^k + \partial_x \varepsilon_p^k + Q(u^k) \right\}$.

Q measures the projection error of a polynomial of degree N to a polynomial of degree $N - 1$. Since u is bounded, this value has also to be bounded. Since (19) and $\kappa \rightarrow 0$, the interpolation error ε_p^k converges in N to zero, provided that $m > 1$ and that the Sobolev norm of the solution is uniformly bounded in time. Therefore, we also need the initial and boundary conditions in the model problem (10). For the time derivative, we get the boundedness of the norm by the relation $\partial_t u = -\partial_x u$. The term $\varepsilon_{2,\varphi}^k$ is bounded, because u is bounded and also continuous. For the numerical fluxes, this value describes the error between the interpolation polynomial at -1 and 1 , as well as the numerical approximation by the numerical flux function at these boundaries. From a different perspective, this value can also be interpreted as the additional dissipation which is added in the Gauß-Legendre case, since for Gauß-Lobatto nodes this error term is zero. This discussion yields that the right side of (39) is well-defined.

Now, we derive the error equation for ε_1^k . We apply the SBP property (4), $\underline{\mathbf{C}} = \left(\underline{\mathbf{M}} + \underline{\mathbf{K}} \right)^{-1} \underline{\mathbf{R}}^T \underline{\mathbf{B}}$ and the property of (8) to equation (22) and obtain

$$\frac{\Delta x_k}{2} \left(\partial_t \underline{u}^k, \underline{\varphi}^k \right)_{M+\tilde{\mathbf{K}}} + \underline{\varphi}^{T,k} \underline{\mathbf{R}}^T \underline{\mathbf{B}} \underline{\mathbf{f}}^{\text{num},k} \left(\left(U^k \right)^-, \left(U^k \right)^+ \right) - \left(\underline{u}^k, \partial_\xi \underline{\varphi}^k \right)_{M+\tilde{\mathbf{K}}} = 0.$$

⁷ The projection operator is defined by the classical truncated Fourier series $P_{N-1}^m u = \sum_{j=0}^{N-1} \hat{u}_j \Phi_j$ up to order $N - 1$ where (broken) Sobolev type orthogonal polynomials $\{\Phi_k\}$ are used as basis function in the underlying space. Essential is that it projects u unto \mathbb{P}^{N-1} and having the representation (8) in mind. For more details about the projection operator and about approximation results, we strongly recommend [6].

We subtract this equation from (39) and by the linearity of the numerical flux, we get an equation for the error $\varepsilon_1^k = \mathbb{I}^N(u^k) - U^k$. It becomes:

$$\begin{aligned} & \frac{\Delta x_k}{2} \left(\partial_t \left(\mathbb{I}^N(u^k) - \underline{u}^k \right), \underline{\varphi}^k \right)_{M+\tilde{K}} + \underline{\varphi}^{T,k} \underline{R}^T \underline{B} \underline{f}^{\text{num},k} \left(\left(\mathbb{I}^N(u^k) - U^k \right)^-, \left(\mathbb{I}^N(u^k) - U^k \right)^+ \right) \\ & - \left(\left(\mathbb{I}^N(u^k) - \underline{u}^k \right), \partial_\xi \underline{\varphi}^k \right)_{M+\tilde{K}} = \frac{\Delta x_k}{2} \langle T^k(u), \varphi^k \rangle + \frac{\Delta x_k}{2} \left(\underline{Q}(u^k), \underline{\varphi}^k \right)_{M+\tilde{K}} - \varepsilon_{2,\varphi}^k, \\ \Leftrightarrow & \frac{\Delta x_k}{2} \left(\partial_t \underline{\varepsilon}_1^k, \underline{\varphi}^k \right)_{M+\tilde{K}} + \underline{\varphi}^{T,k} \underline{R}^T \underline{B} \underline{f}^{\text{num},k} \left(\left(\varepsilon_1^k \right)^-, \left(\varepsilon_1^k \right)^+ \right) - \left(\underline{\varepsilon}_1^k, \partial_\xi \underline{\varphi}^k \right)_{M+\tilde{K}} \\ & = \frac{\Delta x_k}{2} \langle T^k(u), \varphi^k \rangle + \frac{\Delta x_k}{2} \left(\underline{Q}(u^k), \underline{\varphi}^k \right)_{M+\tilde{K}} - \varepsilon_{2,\varphi}^k, \end{aligned}$$

where we can write for the term $\left(\underline{\varepsilon}_1^k, \partial_\xi \underline{\varphi}^k \right)_{M+\tilde{K}} = \left(\underline{\varepsilon}_1^k, \partial_\xi \underline{\varphi}^k \right)_N$ because of (8). Putting $\varphi^k = \varepsilon_1^k$, we obtain the energy equation

$$\begin{aligned} & \frac{\Delta x_k}{4} \frac{d}{dt} \|\varepsilon_1^k\|_{M+\tilde{K}}^2 + \underline{\varepsilon}_1^{k,T} \underline{R}^T \underline{B} \underline{f}^{\text{num},k} \left(\left(\varepsilon_1^k \right)^-, \left(\varepsilon_1^k \right)^+ \right) - \left(\underline{\varepsilon}_1^k, \partial_\xi \underline{\varepsilon}_1^k \right)_N \\ & = \frac{\Delta x_k}{2} \langle T^k(u), \varepsilon_1^k \rangle + \frac{\Delta x_k}{2} \left(\underline{Q}(u^k), \underline{\varepsilon}_1^k \right)_{M+\tilde{K}} - \tilde{\varepsilon}_2^k, \end{aligned}$$

with $\tilde{\varepsilon}_2^k = \left(\varepsilon_1^k \mathbb{I}^N(u^k) \Big|_{-1}^1 - \underline{\varepsilon}_1^{k,T} \underline{R}^T \underline{B} \underline{f}^{\text{num},k} \left(\mathbb{I}^N(u^k)^-, \mathbb{I}^N(u^k)^+ \right) \right)$. Summation-by-parts yields for ε_1^k

$$\begin{aligned} \left(\underline{\varepsilon}_1^k, \partial_\xi \underline{\varepsilon}_1^k \right)_N & = \varepsilon_1^{T,k} \underline{M} \underline{D} \underline{\varepsilon}_1^k = \varepsilon_1^{T,k} \underline{R}^T \underline{B} \underline{R} \underline{\varepsilon}_1^k - \varepsilon_1^{T,k} \underline{D}^T \underline{M} \underline{\varepsilon}_1^k, \\ \Leftrightarrow \quad \varepsilon_1^{T,k} \underline{M} \underline{D} \underline{\varepsilon}_1^k & = \frac{1}{2} \varepsilon_1^{T,k} \underline{R}^T \underline{B} \underline{R} \underline{\varepsilon}_1^k, \end{aligned}$$

and we get

$$\begin{aligned} & \frac{\Delta x_k}{4} \frac{d}{dt} \|\varepsilon_1^k\|_{M+\tilde{K}}^2 + \varepsilon_1^{k,T} \underline{R}^T \underline{B} \left(\underline{f}^{\text{num},k} \left(\left(\varepsilon_1^k \right)^-, \left(\varepsilon_1^k \right)^+ \right) - \frac{1}{2} \underline{R} \underline{\varepsilon}_1^k \right) \\ & = \frac{\Delta x_k}{2} \langle T^k(u), \varepsilon_1^k \rangle + \frac{\Delta x_k}{2} \left(\underline{Q}(u^k), \underline{\varepsilon}_1^k \right)_{M+\tilde{K}} - \tilde{\varepsilon}_2^k. \end{aligned}$$

We have split our equation into a continuous and a discrete part. Coming to step three of our investigation, we sum up over all elements and obtain

$$\begin{aligned} & \frac{1}{2} \frac{d}{dt} \sum_{k=1}^K \frac{\Delta x_k}{2} \|\varepsilon_1^k\|_{M+\tilde{K}}^2 + \sum_{k=1}^K \varepsilon_1^{k,T} \underline{R}^T \underline{B} \left(\underline{f}^{\text{num},k} - \frac{1}{2} \underline{R} \underline{\varepsilon}_1^k \right) \\ & = \sum_{k=1}^K \left(\frac{\Delta x_k}{2} \left(\langle T^k(u), \varepsilon_1^k \rangle + \left(\underline{Q}(u^k), \underline{\varepsilon}_1^k \right)_{M+\tilde{K}} \right) - \tilde{\varepsilon}_2^k \right), \end{aligned} \tag{40}$$

where $\underline{\varepsilon}_1^{\text{num},k} := \underline{f}^{\text{num},k} \left(\left(\varepsilon_1^k \right)^-, \left(\varepsilon_1^k \right)^+ \right)$. This equation has the same form as (26) except the right hand side. We estimate the bracket on the right hand side by the Cauchy-Schwarz inequality. It is

$$\begin{aligned} \tilde{R} & = \sum_{k=1}^K \frac{\Delta x_k}{2} \left(\langle T^k(u), \varepsilon_1^k \rangle + \left(\underline{Q}(u^k), \underline{\varepsilon}_1^k \right)_{M+\tilde{K}} \right) \\ & \leq \sqrt{\sum_{k=1}^K \frac{\Delta x_k}{2} \|T^k(u)\|^2} \sqrt{\sum_{k=1}^K \frac{\Delta x_k}{2} \|\varepsilon_1^k\|^2} + \sqrt{\sum_{k=1}^K \frac{\Delta x_k}{2} \|\underline{Q}(u^k)\|_{M+\tilde{K}}^2} \sqrt{\sum_{k=1}^K \frac{\Delta x_k}{2} \|\underline{\varepsilon}_1^k\|_{M+\tilde{K}}^2}. \end{aligned}$$

With the global norm over all elements and the equivalence between the continuous and discrete norms, we obtain

$$\tilde{R} \leq \left\{ c\|T\| + \|Q\|_{\tilde{K}_M} \right\} \|\varepsilon_1\|_{\tilde{K}_M} =: \tilde{\mathbb{E}}(t) \|\varepsilon_1\|_{\tilde{K}_M}. \quad (41)$$

Using estimation (41) in (40), we get an inequality for the global energy equation for the total error. It is

$$\frac{1}{2} \frac{d}{dt} \|\varepsilon_1\|_{\tilde{K}_M}^2 + \sum_{k=1}^K \underline{\varepsilon}_1^{k,T} \underline{R}^T \underline{B} \left(\underline{\varepsilon}_1^{\text{num},k} - \frac{1}{2} \underline{R} \underline{\varepsilon}_1^k \right) \leq \tilde{\mathbb{E}}(t) \|\varepsilon_1\|_{\tilde{K}_M} - \underbrace{\sum_{k=1}^K \tilde{\varepsilon}_2^k}_{:=\Theta_2} \quad (42)$$

with $\tilde{\varepsilon}_2^k = \left(\varepsilon_1^k \mathbb{I}^N(u^k) \Big|_{-1}^1 - \underline{\varepsilon}_1^{k,T} \underline{R}^T \underline{B} f^{\text{num},k} \left(\mathbb{I}^N(u^k)^-, \mathbb{I}^N(u^k)^+ \right) \right)$. Applying the same approach like in [24, 31] and splitting the sum on the left side into three parts (one for the left physical boundary, one for the right physical boundary) and summing over the internal element endpoints), we get

$$\begin{aligned} & \sum_{k=1}^K \underline{\varepsilon}_1^{k,T} \underline{R}^T \underline{B} \left(\underline{\varepsilon}_1^{\text{num},k} - \frac{1}{2} \underline{R} \underline{\varepsilon}_1^k \right) = \sum_{k=1}^K \underline{\varepsilon}_1^{k,T} \underline{R}^T \underline{B} \left(f^{\text{num},k} \left((\varepsilon_1^k)^-, (\varepsilon_1^k)^+ \right) - \frac{1}{2} \underline{R} \underline{\varepsilon}_1^k \right) \\ & = -\mathbf{E}_L^1 \left(f_L^{\text{num},1} - \frac{1}{2} \mathbf{E}_L^1 \right) + \sum_{k=2}^K \left(f_L^{\text{num},k} - \frac{1}{2} (\mathbf{E}_R^{k-1} + \mathbf{E}_L^k) \right) (\mathbf{E}_R^{k-1} - \mathbf{E}_L^k) \\ & + \mathbf{E}_R^K \left(f_R^{\text{num},K} - \frac{1}{2} \mathbf{E}_R^K \right). \end{aligned}$$

We describe with \mathbf{E}_i ($i = L, R$) the approximated error ε_1 and we have $f_L^{\text{num},k} := f^{\text{num},k}(\mathbf{E}_R^{k-1}, \mathbf{E}_L^k)$, $f_L^{\text{num},1} := f^{\text{num},1}(0, \mathbf{E}_L^1)$ and $f_R^{\text{num},K} := f^{\text{num},1}(\mathbf{E}_R^K, 0)$. The external states for the physical boundary contributions are zero because $\mathbb{I}^N(u^1) = g$ at the left boundary. The external state for U^1 is set to g . At the right boundary, where the upwind numerical flux is used, it does not matter what we set for the external state because its coefficients in the numerical solution is zero. We get for the inner element with $\llbracket \mathbf{E}^k \rrbracket = \mathbf{E}_R^{k-1} - \mathbf{E}_L^k$;

$$\sum_{k=2}^K \left(f_L^{\text{num},k} - \frac{1}{2} (\mathbf{E}_R^{k-1} + \mathbf{E}_L^k) \right) (\mathbf{E}_R^{k-1} - \mathbf{E}_L^k) = \sum_{k=2}^K \frac{\sigma}{2} \left(\llbracket \mathbf{E}^k \rrbracket \right)^2 \geq 0, \quad \text{with } \begin{cases} \sigma = 0 & \text{central flux,} \\ \sigma = 1 & \text{upwind flux.} \end{cases}$$

For the left and right boundaries, we finally get

$$\begin{aligned} \text{left:} \quad & -\mathbf{E}_L^1 \left(f_L^{\text{num},1} - \frac{1}{2} \mathbf{E}_L^1 \right) = -\mathbf{E}_L^1 \left(\left(\frac{0 + \mathbf{E}_L^1}{2} - \sigma \frac{\mathbf{E}_L^1}{2} \right) - \frac{\mathbf{E}_L^1}{2} \right) = \frac{\sigma}{2} (\mathbf{E}_L^1)^2, \\ \text{right:} \quad & \mathbf{E}_R^K \left(f_R^{\text{num},K} - \frac{1}{2} \mathbf{E}_R^K \right) = \mathbf{E}_R^K \left(\left(\frac{0 + \mathbf{E}_R^K}{2} + \frac{1}{2} \sigma \mathbf{E}_R^K \right) - \frac{\mathbf{E}_R^K}{2} \right) = \frac{\sigma}{2} (\mathbf{E}_R^K)^2. \end{aligned}$$

Therefore, the energy growth rate is bounded by

$$\frac{1}{2} \frac{d}{dt} \|\varepsilon_1\|_{\tilde{K}_M}^2 + \underbrace{\frac{\sigma}{2} \left((\mathbf{E}_R^K)^2 + (\mathbf{E}_L^1)^2 \right) + \frac{\sigma}{2} \sum_{k=2}^K \left(\llbracket \mathbf{E}^k \rrbracket \right)^2}_{BTs} \leq \tilde{\mathbb{E}}(t) \|\varepsilon_1\|_{\tilde{K}_M} - \Theta_2. \quad (43)$$

The term BTs is bigger than or equal to zero depending on the used fluxes. The energy growth inequality (43) is similar to the inequality in [24]. The differences are the used norms and the term Θ_2 which will yield

a smaller upper bound under the condition $\Theta_2 \geq 0$. We follow the steps in [24, 27] and get

$$\frac{\partial}{\partial t} \|\varepsilon_1\|_{\tilde{K}_M} + \underbrace{\frac{BTs + \Theta_2}{\|\varepsilon_1\|_{\tilde{K}_M}^2}}_{\eta(t)} \|\varepsilon_1\|_{\tilde{K}_M} \leq \tilde{\mathbb{E}}(t). \quad (44)$$

Like it was described in [27], we have to assume that the mean value of $\eta(t)$ is bounded by a positive constant δ_0 from below. This means that $\bar{\eta} \geq \delta_0 > 0$. Under the assumption on u , the right hand side $\tilde{\mathbb{E}}(t)$ is bounded in time and we can put $\max_{t \in [0, \infty)} \tilde{\mathbb{E}}(t) \leq C_1 < \infty$. Applying these facts in (44), we integrate over the time and get the following inequality for the error

$$\|\varepsilon_1(t)\|_{\tilde{K}_M} \leq \frac{1 - \exp(-\delta_0 t)}{\delta_0} C_1, \quad (30)$$

see [27, Lemma 2.3] for details. If $\Theta_2 > 0$, the existence of δ_0 is actually met without restrictions. On the physical boundaries, we apply always the upwind flux ($\sigma = 1$). Therefore, we may modify the BTs term in (43) and we have

$$BTs = \frac{1}{2} \left((\mathbf{E}_R^K)^2 + (\mathbf{E}_L^1)^2 \right) + \frac{\sigma}{2} \sum_{k=2}^K (\mathbf{E}^k)^2 > 0.$$

In case that $BT > -\Theta_2$ the assumption on the existence of a positive constant δ_0 is therefore always fulfilled. We transferred the results from [24, 27] to the more general case of the one parameter family of Vincent et al. (8) and extended the basis also to Gauß-Legendre. We may conclude:

If the truncation error is bounded, the dissipative boundary conditions keep also the error bounded in time for both Gauß-Lobatto as well as Gauß-Legendre nodes. The selections of basis and numerical fluxes have an essential influence on the error behaviour.

In [24, p.325] their model⁸ (30) yields the authors the following predictions:

- P1 *Using the upwind flux at the physical boundaries and either the upwind flux or the central flux at the interior element interfaces, the error growth is bounded asymptotically in time.*
- P2 *Using the upwind flux $\sigma = 1$ in the interior will lead to a smaller asymptotic error than using the central flux, $\sigma = 0$. This will be especially true for under-resolved approximations.*
- P3 *As the resolution increases, the difference between the asymptotic error from the central and upwind fluxes should decrease.*
- P4 *The error growth rate will be larger when the upwind flux is used compared to when the central flux is used. Equivalently, the upwind flux solution should approach its asymptotic value faster than the central flux solution.*

Through our investigation in this section and by the model (30), these predictions are also valid using Gauß-Legendre nodes and we can extend these by the following:

- P5 *The error should be larger when Gauß-Lobatto nodes are used compared to when a Gauß-Legendre basis is applied.*

Applying Gauß-Legendre nodes is more accurate than using Gauß-Lobatto nodes. Therefore, the norm of the ε_1 -error is smaller by utilizing a Gauß-Legendre basis. This leads directly to a bigger value of $\bar{\eta}$ and thus to a bigger δ_0 in (30). Furthermore, the ε_2 -error may have a positive effect on the error behavior.

- P6 *By using Gauß-Legendre nodes, the choice of the numerical fluxes should be less important than in the Gauß-Lobatto case.*

This is a direct consequence of P3 and P5.

⁸Using Gauß-Lobatto nodes and investigating the DGSEM (i.e. $\kappa = 0$ in (8)).

P7 *By applying a FR scheme with $\kappa \neq 0$, the errors should show some oscillations.*

For $\kappa \neq 0$, the correction term with $\tilde{K} \neq 0$ works directly on the highest degree monomials in U with different strength which leads to oscillations. As it is shown in [3], the correction functions (8) correspond to top-mode filters of different strengths.

Remark 5.3. If $\Theta_2 \geq 0$, the term can be seen as an additional dissipation term which is added in the Gauß-Legendre case and lead to a smaller upper bound. Furthermore, because of the construction of $\tilde{\varepsilon}_2$ and the evaluation at the boundaries, we suppose that the ε_1 error has a direct influence on the behavior of $\tilde{\varepsilon}_2$ and we also get some noisy behavior. Finally, it is

$$\tilde{\varepsilon}_2^k = \varepsilon_1^{k,T} \underline{R}^T \underline{B} \left(\underline{R} \mathbb{I}^N(u^k) - \underline{f}^{\text{num},k} \left(\mathbb{I}^N(u^k)^-, \mathbb{I}^N(u^k)^+ \right) \right).$$

The term in the bracket describes the error between the flux function and the numerical flux function at the element boundaries. In case of a consistent numerical flux these terms tend to zero under mesh refinement and/or increasing the polynomial order of the approximation. This can be shown by Taylor series expansion but is not the topic here. In the next section, the term $\tilde{\varepsilon}_2$ will be investigated numerically.

In our investigation, we apply the discrete norms (21) of the one parameter family of Vincent et al. and we assume in 2.2 that κ in (21) tends rapidly to zero if we increase the polynomial order N . The nowadays main used FR schemes (presented in table 1) fulfill the assumption 2.2. The first term in the norm is the essential one. For the norm of the interpolation error $\|\varepsilon_p^k\|_{\tilde{K}+M}$, we estimate the first part by (17)-(18) and due to assumption 2.2 we may neglect the terms of the interpolation errors in the investigation. Nevertheless, the stability analysis of [38] allows κ to tend to infinity. Therefore, in the case $\kappa \rightarrow \infty$ a more detailed analysis is necessary. We may estimate the second part of the norm (21) using Bernstein inequality together with estimation (17), or directly (18).

A further investigation about the approximation behavior concerning limit processes of $K, N, m, \kappa \rightarrow \infty$ would be indeed desirable for this case. Both is beyond the scope of this paper where the influence of the flux functions and nodal bases is investigated.

We want to point out that spectral convergence is always investigated under the requirement that our solution u is C^∞ and m from (18) tends to infinity for all orders of accuracy [6]. It is clear that our approach can be easily transformed to multidimensional problems using a tensor product structure on structured grids.

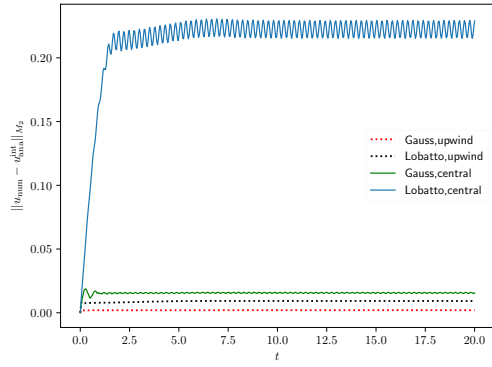
6 Numerical Tests

In this section we consider numerical tests which demonstrate both the error bound (30) and confirms our predictions. The usage of a tensor product structure to consider multidimensional problems does not lead to more information or further observations for our model problem as the one-dimensional setting. This is the reason why we limit ourself to the one-dimensional case. We do not only apply Gauß-Lobatto nodes, but also employ a Gauß-Legendre basis. Our numerical simulations confirm our observation from remark 5.3 that the error term $\tilde{\varepsilon}_2^k$ may have a positive effect on the numerical scheme, and we get more accurate solutions by using a Gauß-Legendre basis. Also the influence of the different numerical fluxes is less important than in the Gauß-Lobatto case, especially if we chose the SBP-FR methods with $\underline{C} = \underline{M}^{-1} \underline{R}^T \underline{B}$ for the space discretization.

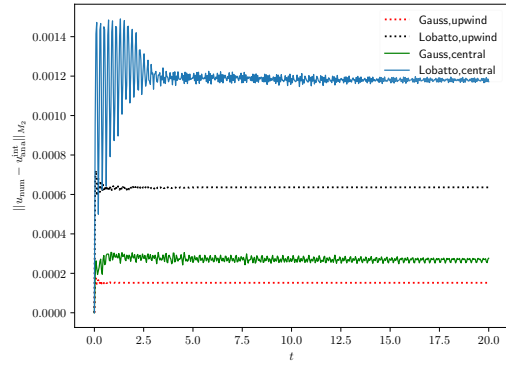
Simultaneously, results about the error behavior of several other correction terms \underline{C} will be given. The numerical schemes of table 1 and multiples of them will be considered. We present several examples which justify our observations, but also show some limitations of our results.

We use an upwind flux (dotted lines) and central flux (straight lines) at the interior element interfaces⁹. For time integration we use in all numerical examples a SSPRK(3,3) where the time step is chosen in such way that the time integration error is negligible. All elements are of uniform size.

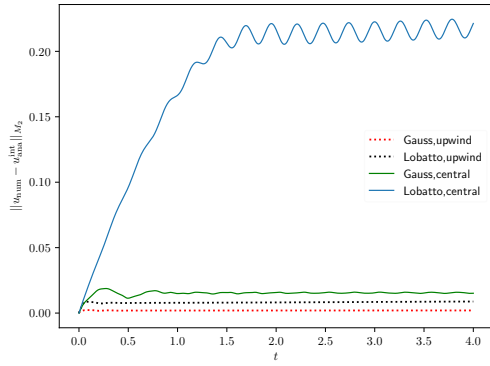
⁹We apply always an upwind flux at the physical boundaries.



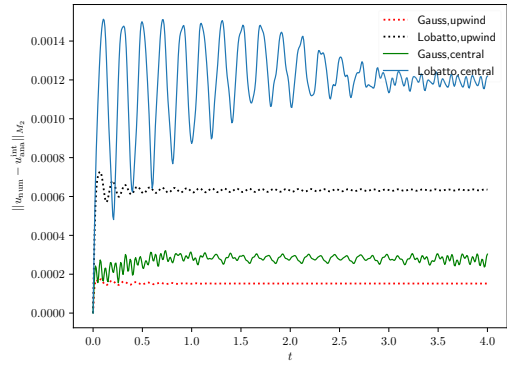
(a) $N = 4, K = 30, t = 20$



(b) $N = 4, K = 50, t = 20$



(c) $N = 4, K = 30, t = 4$



(d) $N = 4, K = 50, t = 4$

Figure 1: Error as a function in time. The dashed lines are always the calculation with the upwind flux. Left side less elements than right. (c) and (d) early time behavior.

6.1 Error behavior

Sine-Testcase

We start our numerical section with the same example as in [24, p. 32]. We analyze the error behavior for $L = 2\pi$ and the initial condition $u_0 = \sin(12(x - 0.1))$, with the boundary condition $g(t)$ chosen so that the exact solution is $u(x, t) = \sin(12(x - t - 0.1))$. In figure 1 we illustrate the discrete errors over time for different number of elements with a fourth order polynomial approximation. The errors are always bounded in time for all combinations (P1) (upwind / central flux and Gauß-Lobatto / Gauß-Legendre basis). We realize that the upwind flux errors reach its asymptotic values faster than the central flux errors in all cases (P4). Simultaneously, the error bounds for the central flux are larger than for the upwind flux (P2). These results have already been seen in [24] (in case of Gauß-Lobatto nodes), together with the fact that the central flux errors are noisier than the upwind flux in all observations for all of the meshes and polynomial orders. Here, we make the following two *new* observations which confirms our (new) predictions.

The error bounds using Gauß-Lobatto points are larger than in the Gauß-Legendre case (P5), and secondly the influence of the different numerical fluxes is less important than in the Gauß-Lobatto case (P6). Besides the accuracy properties of the different bases, the error term $\tilde{\varepsilon}_2$ has also a positive effect on the total error, and we get a more accurate solution in this case, see remark 5.3. Gauß-Legendre nodes do not include the points at the element interfaces. The additional dissipation comes from his fact and so the influence of the dissipation from the upwind flux is less important compared to the Gauß-Lobatto case. If we increase the order of approximation, the error bounds of the different combinations should coincide. The figure 2 justifies this prediction (P3).

Last, but not least, we also study the convergence speed and observe spectral accuracy in all cases, see figure 3. This suggests that the approximation errors in $\mathbb{E}(t)$ decay faster than $\frac{1}{\delta_0}$ grows, since with inequality (30) one predicts that the time asymptotic error is bounded by $\mathbb{E}(t)/\delta_0$. This matches also with the investigation in [24].

We are not only considering the FR scheme which is equivalent to the DG framework. We also investigate the schemes of Huynh and the SD methods.

The correction terms are written in table 1 and we demonstrate the error behaviors in figure 4 using the $\|\cdot\|_{\tilde{K}_M}$ -norm and the global norm (15). We realize that the error is always bounded in all cases (P1) and, indeed, that the influence of the numerical flux is less important comparing to the chosen basis function ((P5) and (P6)). Here, the usage of Gauß-Legendre nodes demonstrates their good advantage comparing to the usage of Gauß-Lobatto nodes (P5). Nevertheless, we make also one more observation in this case. Different from the DG case, our errors show always some oscillations even using the upwind flux (P7). This can be seen in figure 5 where only Gauß-Legendre nodes are considered. This is due to the fact that using another correction term as for the case $\kappa = 0$, we get some *over correction* and *under correction* at the boundaries through our correction functions. It is not surprising that by using Gauß-Lobatto nodes and a central flux we get the worst simulation if the resolution is low order (P1-P7).

If we decrease the correction terms more rapidly to zero, we obtain some intermediate schemes on the way to the DG case ($\kappa = 0$). In figure 6, we plot the SD method and Huynh scheme by dividing the correction terms with 2^{N-1} . We see that these simulations behave like our first test (figure 1) except with noisier behavior. We also realize that using Gauß-Legendre nodes, the scheme demonstrates a higher amplitude in the oscillations and, therefore, the Gauß-Lobatto nodes seem better (more about this in section 6.2).

Cosine-Testcase

As a second testcase, we investigate the error behavior for $L = 2\pi$ and the initial condition $u_0 = \cos(12(x - 0.1))$, with the boundary condition $g(t)$ chosen so that the exact solution is $u(x, t) = \cos(12(x - t - 0.1))$. With this testcase we want to strengthen our conclusions from before.

In figure 7 we illustrate the discrete errors over time for different number of elements with a fourth and sixth order polynomial approximation. We make equivalent observations like before and see that using Gauß-Legendre nodes in our scheme yields more accurate solutions than when using Gauß-Lobatto nodes

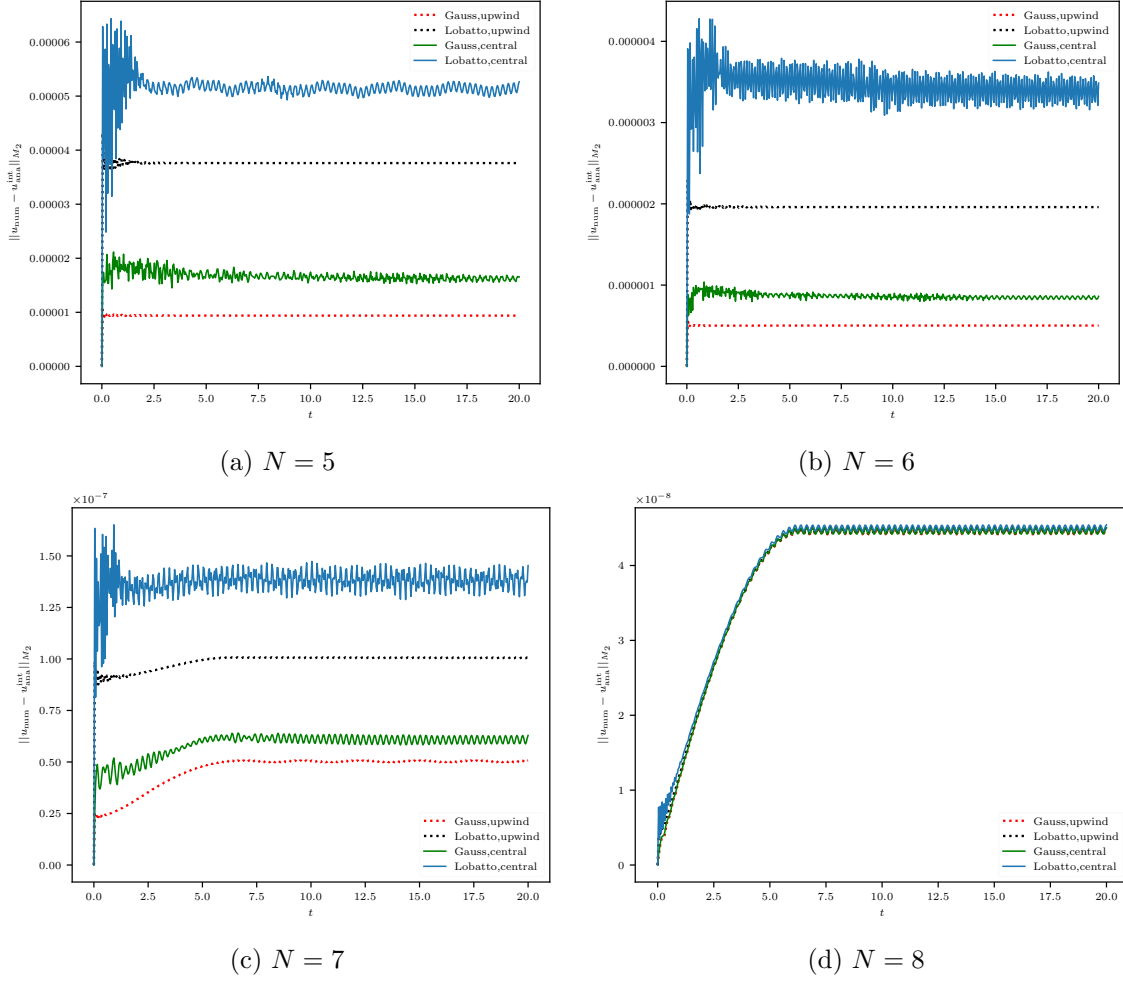


Figure 2: Error as a function in time. The dashed lines are always the calculation with the upwind flux. $K = 50$ and $t = 20$.

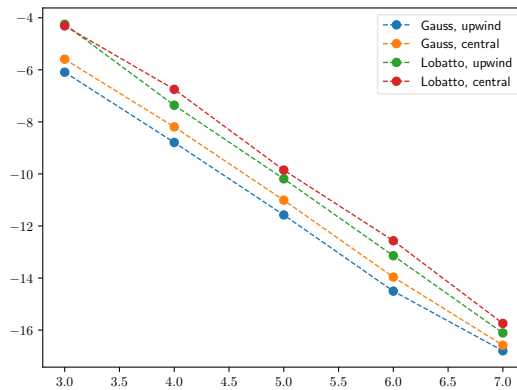
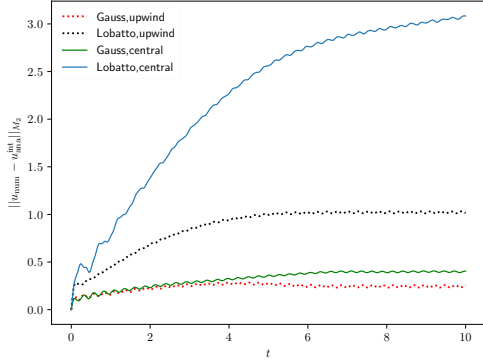
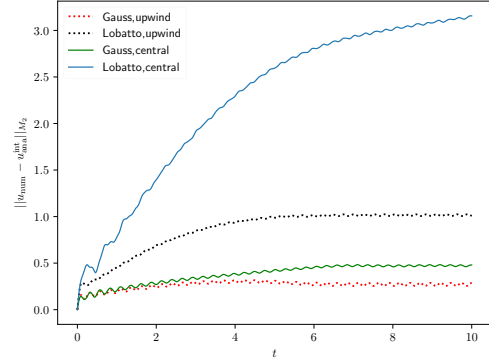


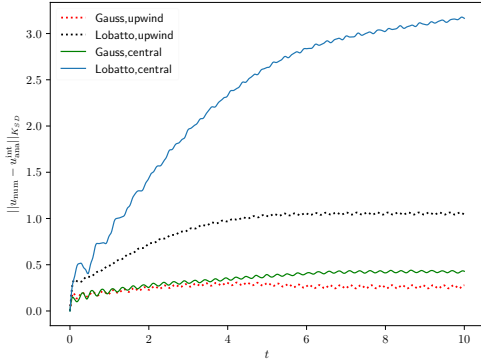
Figure 3: Convergences in time asymptotic errors (last value) as functions of N for $K = 50$.



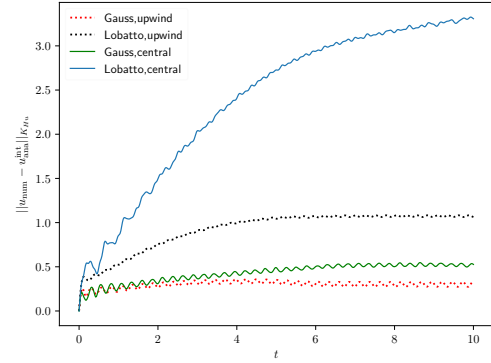
(a) $N = 3, K = 20, t = 10$



(b) $N = 3, K = 20, t = 10$



(c) $N = 3, K = 20, t = 10$



(d) $N = 3, K = 20, t = 10$

Figure 4: Error as a function in time. The dashed lines are always the calculation with the upwind flux. Right side SD scheme and on the left side Huynh. (c) and (d) respective \tilde{K}_M -norm.

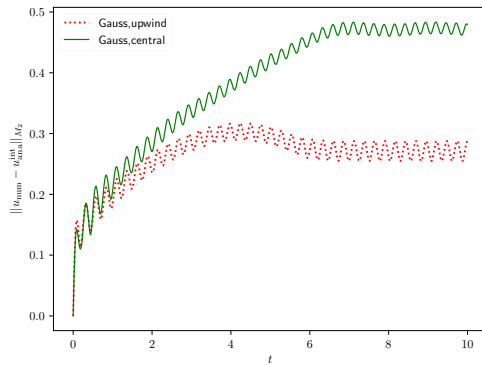
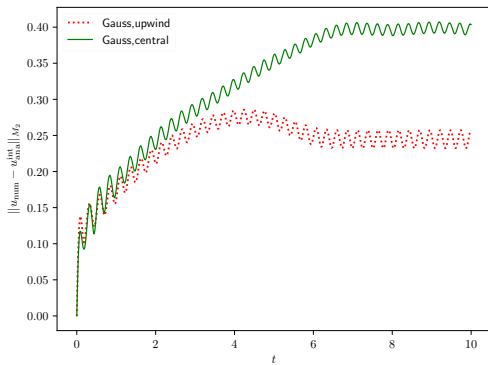


Figure 5: Error as a function in time only with Gauß-Legendre nodes. Left: SD, Right: Huynh

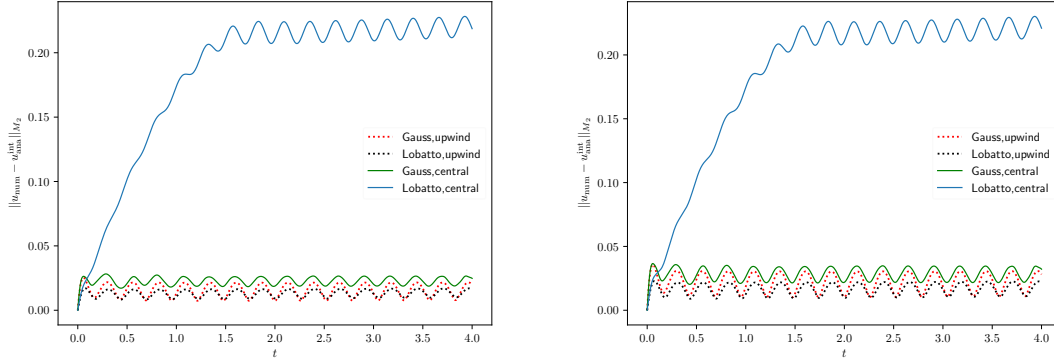
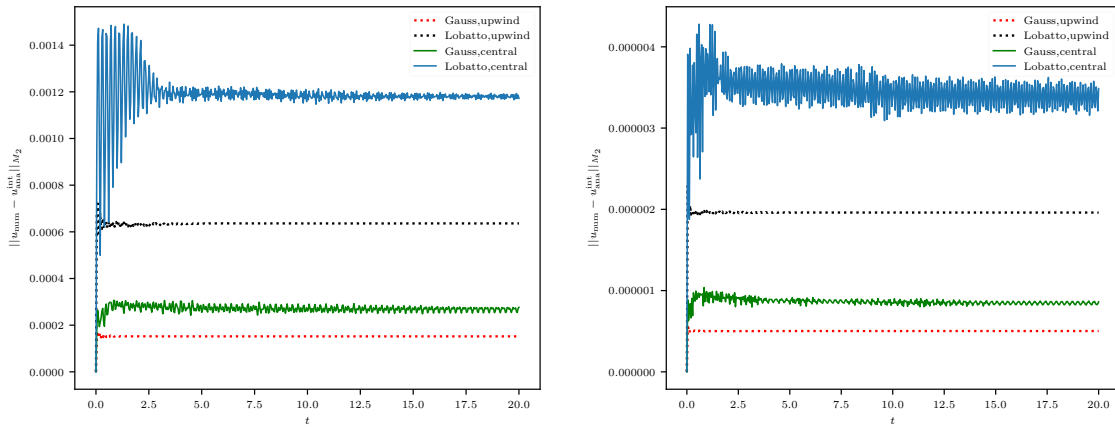


Figure 6: Error as a function in time only with Gauß-Legendre nodes $K = 30$ and $N = 4$. Correction Term: $c_{SD}/2^{N-1}$ (left), $c_{Hu}/2^{N-1}$ (right)



(a) $N = 4$

(b) $N = 6$

Figure 7: Error as a function in time with 50-elements.

(P5). Also, the difference between the upwind flux error and central flux error is not so large (P6). The same observations can be made by using the FR schemes from before.

$\tilde{\varepsilon}_2$ -Term

Finally, we study the $\tilde{\varepsilon}_2$ terms for the two testcases. In figure 8, the $\tilde{\varepsilon}_2$ -error is plotted over the time for different polynomial orders as in the sin testcase. Both times the error starts positive for the lower order

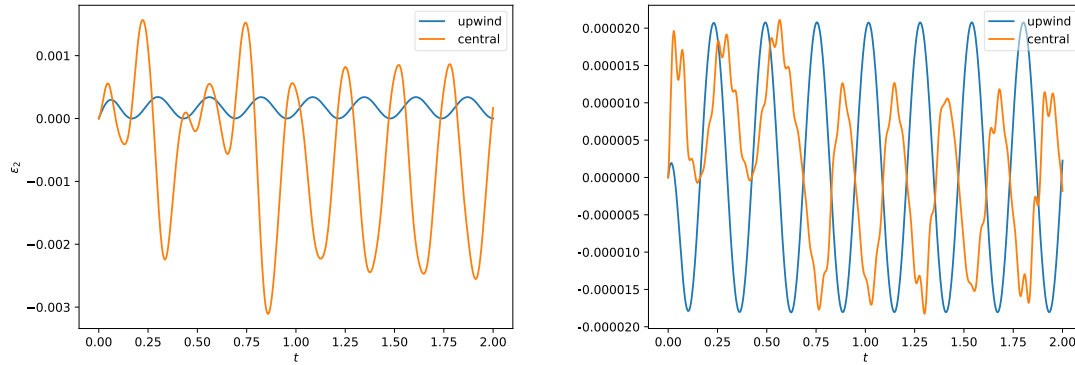


Figure 8: $\tilde{\varepsilon}_2$ a function in time $K = 30$ and $N = 4, 5$.

approximation ($N = 4$), and the upwind flux stays strictly positive whereas the term using the central flux shows a higher amplitude in the oscillations and turns also negative. Even the middle point of the amplitudes is below zero. Since the ε_1 - errors show these oscillations when applying the central flux, we also get them in the $\tilde{\varepsilon}_2$ -terms. This is also not surprising because ε_1 has a direct influence on $\tilde{\varepsilon}_2$. Using a fifth order approximation, the amplitude of the error using the upwind flux shows a higher amount, but these are symmetrical around zero, whereas applying the central flux the symmetric point lies in the negative axis. Comparing the amounts of the total error in figure 1 with figure 8 demonstrates that the $\tilde{\varepsilon}_2$ errors are significantly less, but may have an positive influence, especially if Gauß-Legendre nodes are used. In figure 9 we have an analogous behavior for the cosine testcase. All of these results are consistent with our

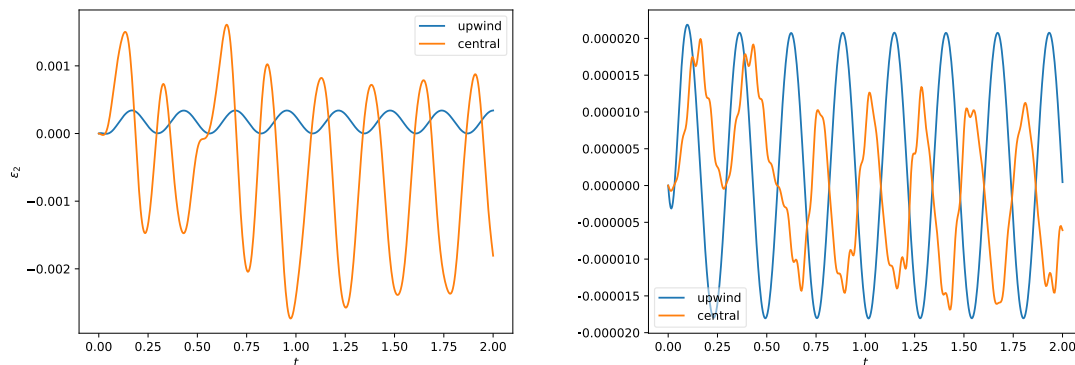


Figure 9: $\tilde{\varepsilon}_2$ a function in time $K = 30$ and $N = 4, 5$.

investigation / predictions from before.

6.2 Limitations and Counterexamples

We make a series of test calculations and most of the time the simulations support our predictions. Nevertheless, there are several examples which question some of the predictions $P2 - P7$. We consider and discuss in the following several examples when $P2$ or $P5$ are not longer correct. At the end, we will give further a counterexample if the solution is not in the assumed space.

P2 is incorrect

We start in our first example with the sine-testcase and use the FR scheme which is equivalent to the DG framework. In the error plot 3, one realizes that the upwind error lies under the central error if a polynomial approximation of order three is used. In fact, we see this clearly in figure (10 (a)). Here, the central error lies above the upwind error, and also the asymptotic state is nearly the same. We assume that the noisy state is *periodic* with the central flux. We may interpret this as using polynomial order 3 in our schemes is too inaccurate for the approximation with the Gauß-Lobatto basis. Then, applying an upwind flux adds too much dissipation into our calculation, and this unpredictable behavior contradicts $P2$. In figure 10 (b), we get a similar error behavior as before if we decrease the number of elements¹⁰ K . With the higher jumps at the element interfaces, the upwind flux yields a more inexact numerical solution. We may conclude that we need an adequate number of elements to get the predicted results in the Gauß-Lobatto case. However, the numerical errors (upwind and central) with the Gauß-Legendre basis show the suspected

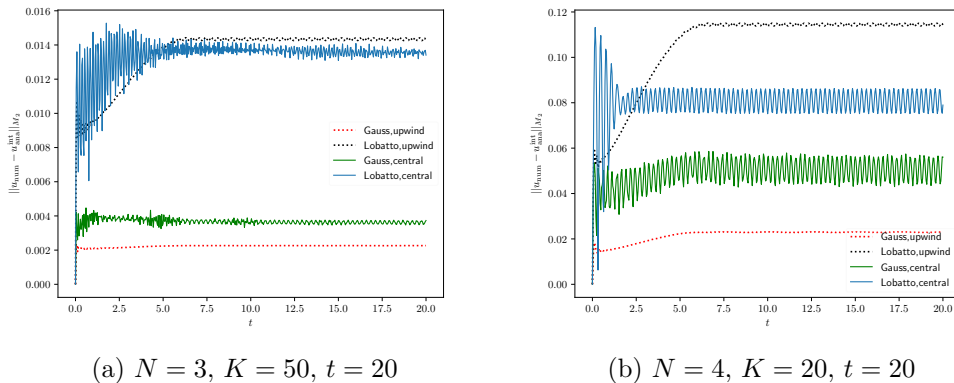


Figure 10: Error as a function in time.

behaviors from our results and one may interpret that as an advantage by using this basis type, but this is not the case. In figure 11 (a) we see the numerical errors of the cosine-case when using polynomial order 3 and 20 elements. Here, the errors applying Gauß-Lobatto nodes behave in accordance to (P2) and the errors with Gauß-Legendre basis do not. We suppose that by using Gauß-Legendre basis and an upwind flux the jumps between the element interfaces is too high and we get this effect. If we again increase the number of elements, and so, the numbers of degrees of freedom, we realize a change in the error behaviors (compare 11 (a)-(c)). Nevertheless, the absolute error when using Gauß-Legendre nodes is comparatively low. This limitation is noticed by focusing on the scheme with the correction matrix $\underline{C} = \underline{M}^{-1} \underline{R}^T \underline{B}$. As it is already known [7, 38, 39], the most accurate results are obtained if $\kappa = 0$. Simultaneously, these results can also be seen as an example of the even-odd phenomena for central fluxes. It is observed in the literature [10, 14, 19, 40] when the numerical flux function at the interface is symmetric (with the central flux), then the convergence order for an order N scheme is $N + 1$ if N is odd, or only N if N is even. If the

¹⁰In [15] the influence of the dispersion and dissipation errors of Gauß-Legendre and Gauß-Lobatto is investigate also in respect to the number of elements.

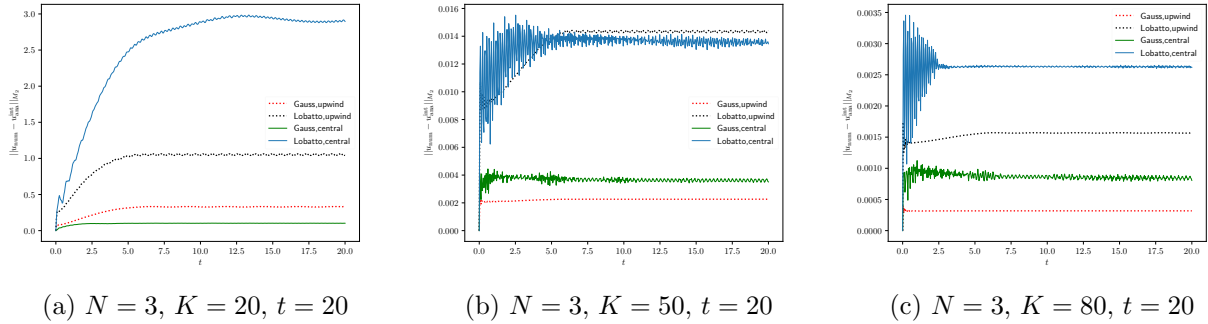


Figure 11: Error as a function in time.

numerical flux adds dissipation, then this even-odd behavior is usually gone. Since the choice of the flux has influence of the convergence order, and it has so on the errors.

P5 is not correct

Nevertheless, for other correction terms we have also some limitations for our prediction P5. Already in figure 6, we realize that error using Gauß-Lobatto nodes and an upwind flux is less compared to the case applying Gauß-Legendre nodes, since the amplitudes of the oscillations are not as high. Indeed, for FR schemes with $\kappa \neq 0$ we have some over and under corrections at the boundaries of every element. If we increase the order or accuracy these amplitudes will decrease and, since the Gauß-Lobatto nodes include the boundaries, it will yield to an error which is equal or less than applying Gauß-Legendre nodes. Simultaneously, we have to realize that using Gauß-Legendre leads, already in low order computations, to comparatively good results (compare figures 6 and 12).

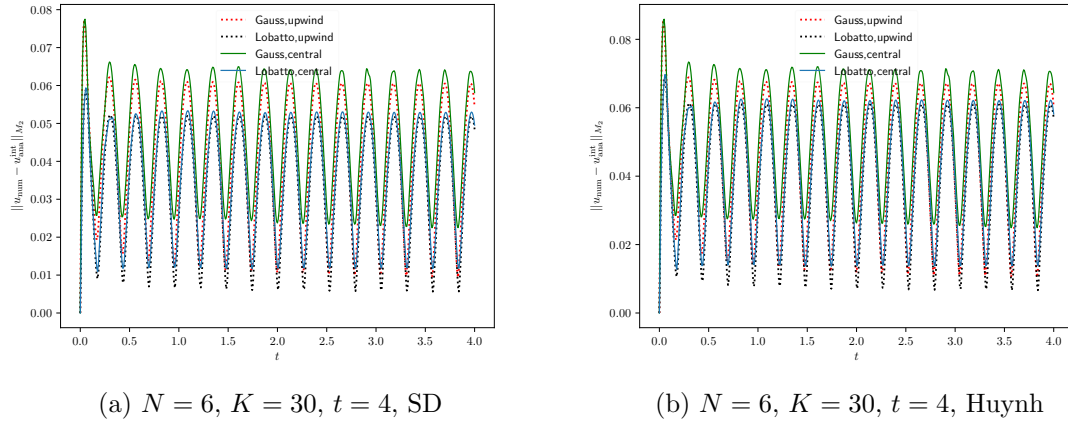
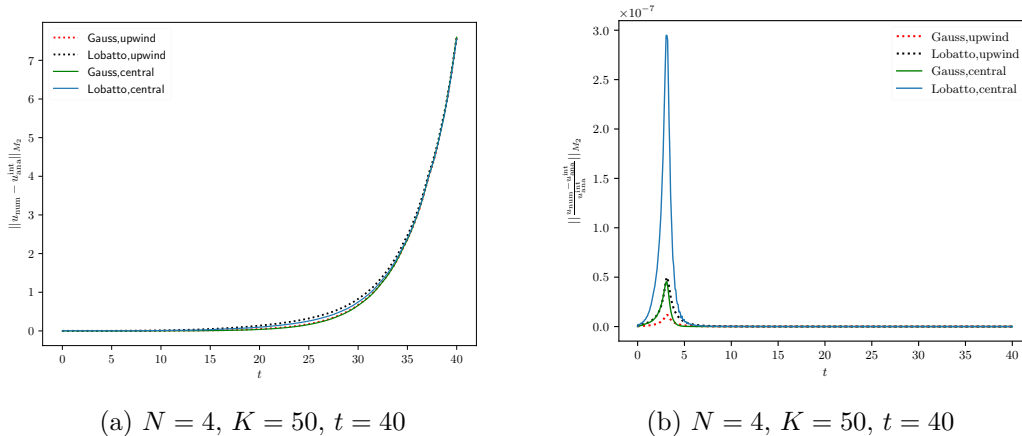


Figure 12: Error as a function in time.

Counterexample

In section 3 we mentioned an example where the norm of solution $\|u\|_{H_{\kappa,N}^m}$ is not uniformly bounded in time. We select our initial and boundary conditions in such way that we get as the solution $u(t, x) = (x - t)^8$.

Using $\kappa = 0$ the figure 13(a) shows the unbounded increase of the errors. However, we have to mention that the relative errors remain bounded 13(b).



(a) $N = 4$, $K = 50$, $t = 40$

(b) $N = 4$, $K = 50$, $t = 40$

Figure 13: Left: Errors as functions in time. Right: Relative errors

7 Summary and Conclusion

In this paper, we transfer the results about the bounded error growth from the discontinuous Galerkin spectral element method [24] to the more general framework of SBP-FR methods. Furthermore, we extend the investigation by including the Gauß-Legendre basis, where [24] considers only the Gauß-Lobatto basis. Indeed, for both bases (Gauß-Lobatto / Gauß-Legendre), the numerical flux used at element boundaries affects the error growth behavior. If an adequate number of elements is used, the upwind flux leads to better results. The asymptotic values are smaller and are reached in a shorter time period. At once, also the selection of basis has a big influence and in our opinion is even more important. Using Gauß-Legendre basis, the error reaches the asymptotic value faster and to a lower value than by using Gauß-Lobatto basis. Also, the impact of the different numerical fluxes (central / upwind) when applying Gauß-Legendre basis is less important than in the Gauß-Lobatto case, especially using a low order polynomial approximation. These effects decrease when the order of polynomial approximation is increased and/or using more elements (which also increase the resolution).

The investigation implies that the usage of Gauß-Legendre basis has some advantages compared to Gauß-Lobatto and should be preferred. However, there are several points which we have to mention yet.

We investigate a trivial model problem (10) where the flux function is simple; $f(u) = u(x, t)$. Already by using the more complicated flux $f(u) = a(x)u(x, t)$ several problems arise in the discretization by using Gauß-Legendre nodes, see [26] for details. The reason is that Gauß-Legendre points do not include the boundary points in one element, and we get some aliasing effect if we are not careful in the discretization. In [34], the author proves a way to solve these issues by applying further correction terms to approximate the boundary terms correctly. Recently, the authors have investigated the long time error behavior of a DG method in this context in [31]. For non-linear flux functions stability problems rise automatically. The aliasing effect is quite stronger and to remedy these issues, further correction terms are needed [35]. By including the boundary points, these correction terms are simpler and better understood. [33] provides the correction terms for the shallow water equation using Gauß-Legendre nodes and recently, the concept of *decoupled SBP* operators introduced by Chan [8] is used to build those correction terms for the Euler equations. The numerical study in [9] demonstrates also some advantages of applying Gauß-Legendre nodes which supports our theoretical analysis here. In our calculations, the time integration analysis was neglected, but in practice it is also an important issue. In [15], the authors already investigate the time-step restriction

by using Gauß-Lobatto or Gauß-Legendre nodes in the DGSEM and find out that Gauß-Lobatto nodes have favored properties.

The above mentioned issues are not unimportant. However, due to our analysis and the numerical results (also in [9]) the usage of Gauß-Legendre basis should be taken into account. In our tests the asymptotic error values are reached faster and to a smaller amount. Nevertheless, further studies are necessary. First, one has to analyze the impact of $\tilde{\varepsilon}_2$ not only numerically but also analytically. Secondly, we must study what happens with the approximation error if the initial conditions have jumps or even more complex flux functions are considered.

8 Appendix

Connection to DG

As it is described several times, there is a close connection between the DG and the FR framework. Therefore, we repeat the main aspect and present one example for a better understanding. FR schemes use in their discretizations of (1) no weak /variational or integral form. A differential form (7) is applied. The main idea of the FR schemes is that the numerical fluxes at the boundaries are corrected by correction functions in such manner that basic properties (e.g. conservation) hold. In [38], the authors develop a class of energy stable FR schemes depending on a single scalar parameter. The correction functions are given for the left and right boundary in one element by the following formula:

$$c_{LB}(\xi) = \frac{(-1)^p}{2} \left[L_p(\xi) - \left(\frac{\lambda_p L_{p-1}(\xi) + L_{p+1}(\xi)}{1 + \lambda_p} \right) \right], \quad c_{RB}(\xi) = \frac{1}{2} \left[L_p(\xi) + \left(\frac{\lambda_p L_{p-1}(\xi) + L_{p+1}(\xi)}{1 + \lambda_p} \right) \right], \quad (45)$$

where L_p is the p -Legendre polynomial and $\lambda_p = \frac{\kappa(p+1)2^{2p}(p!)^4}{((2p)!)^2}$ is a term with the free parameter κ . The translation about these correction functions and our notation can be found in [35].

As mentioned before, we get into the DG framework by selecting $\kappa = 0$. Then, the corrections functions are the right and left Radau polynomials and the application of these polynomials as correction functions is essential. We present the following example from [20, pages 23-25]. We strongly recommend also the review paper [21] where this connection is also pointed out.

Example 8.1. We are considering a scalar conservation law

$$\partial_t u + \partial_x f(u) = 0. \quad (46)$$

A DG formulation for the problem on the standard interval $I = [-1, 1]$ is given by

$$\int_I \frac{\Delta x_k}{2} (\partial_t U) \varphi(\xi) d\xi + \varphi(1) f_{up}^{\text{num}}(1) - \varphi(-1) f_{up}^{\text{num}}(-1) - \int_I \partial_\xi \varphi(\xi) d\xi = 0, \quad (47)$$

where U, F are polynomials that approximate u and f . f_{up}^{num} is the upwind flux and φ is the test function (polynomials of degree N). Instead of solving (47), we want to eliminate the test function φ . Therefore, we apply again integration by parts and reformulate (47) to

$$\int_I \frac{\Delta x_k}{2} (\partial_t U) \varphi(\xi) d\xi + \varphi(1) [f_{up}^{\text{num}}(1) - F(1)] - \varphi(-1) [f_{up}^{\text{num}}(-1) - F(-1)] + \int_I (\partial_\xi F) \varphi(\xi) d\xi = 0. \quad (48)$$

The right and left Radau polynomials of degree $N + 1$ have the property that for any polynomial φ of degree N or less the following equations

$$-\varphi(-1) = \int_{-1}^1 (\partial_\xi c_{LB}(\xi)) \varphi(\xi) d\xi \quad \text{and} \quad \varphi(1) = \int_{-1}^1 (\partial_\xi c_{RB}(\xi)) \varphi(\xi) d\xi \quad (49)$$

are fulfilled. With this property (49) we are able to factor out φ in (48) and obtain

$$\int_I \left(\frac{\Delta x_k}{2} (\partial_t U) + (\partial_\xi \hat{F}) \right) \varphi(\xi) \, d\xi = 0$$

with

$$\hat{F}(\xi) = F(\xi) + [f_{up}^{num}(1) - F(1)]c_{RB}(\xi) + [f_{up}^{num}(-1) - F(-1)]c_{LB}(\xi).$$

Switching to the global coordinate,

$$\int_{x^{k-1}}^{x^k} \left((\partial_t U) + (\partial_x \hat{F}) \right) \varphi(x) \, dx = 0. \quad (50)$$

Since the equation (50) holds for any polynomial φ of degree N , it is equivalent to

$$\partial_t U + \partial_x \hat{F} = 0, \quad (51)$$

which is nothing else than the flux reconstruction scheme with the Radau polynomials as correction functions. Finally, we showed that the DG scheme is equivalent to this FR method.

This connection is also pointed out in the review article [21]. Furthermore, the relation to the DGSEM can also be seen by comparing the work [14] and our introduction in section 2. Here, also the used notations to describe the methods are quite similar.

Stability of FR schemes

Finally, we like to mention that Jameson utilizes in his investigation in [22] a kind of broken Sobolev norm. Let $m \in \mathbb{N}_0$. The norm of the Sobolev space $H^m((-1, 1))$ is given by

$$\|u\|_{H^m((-1,1))} := \left(\sum_{j=0}^m \|u^{(j)}\|_{\mathbf{L}^2((-1,1))}^2 \right)^{\frac{1}{2}},$$

where the derivatives $u^{(j)}$ are taken in a weak sense. In [22], the norm

$$\|u\|_{H_{\kappa,N}((-1,1))}^2 := \int_{-1}^1 u^2 + \kappa (u^{(N)})^2 \, d\xi, \quad (52)$$

is used. Here, N represents the order of accuracy. The solution space (a polynomial space) is equipped with the norm (52) and linear stability is studied in this context. This norm is also used in [38] where the one-parameter family of FR schemes is developed, the correction functions (45) are defined, and coefficients κ are determined to embed the known schemes into their setting.

As it can be found in [38], the nodal DG framework is obtained by selecting $\kappa \equiv 0$. For spectral difference and Huynh scheme, we have

$$\kappa_{SD}(N) = \frac{2N}{(2N+1)(N+1)(a_N N!)^2} \quad \text{and} \quad \kappa_{Hu}(N) = \frac{2(N+1)}{(2N+1)N(a_N N!)^2}.$$

These formulas have been used to calculate the values in table 1. Instead of working with this continuous broken Sobolev norm (52) from [22], we apply the discrete counterpart and use this in our investigation. More details can be found in [35].

References

- [1] S. Abarbanel, A. Ditkowski, and B. Gustafsson. On error bounds of finite difference approximations to partial differential equations—temporal behavior and rate of convergence. *Journal of Scientific Computing*, 15(1):79–116, 2000.
- [2] R. Abgrall, E. I. Meledo, and P. Öffner. On the connection between residual distribution schemes and flux reconstruction. *arXiv preprint arXiv:1807.01261*, 2018.
- [3] Y. Allaneau and A. Jameson. Connections between the filtered discontinuous Galerkin method and the flux reconstruction approach to high order discretizations. *Computer Methods in Applied Mechanics and Engineering*, 200(49):3628–3636, 2011.
- [4] C. Bernardi and Y. Maday. Properties of some weighted Sobolev spaces and application to spectral approximations. *SIAM journal on numerical analysis*, 26(4):769–829, 1989.
- [5] C. Bernardi and Y. Maday. Polynomial interpolation results in Sobolev spaces. *Journal of computational and applied mathematics*, 43(1-2):53–80, 1992.
- [6] C. Canuto, M. Y. Hussaini, A. M. Quarteroni, A. Thomas Jr, et al. *Spectral methods in fluid dynamics*. Springer Science & Business Media, 2012.
- [7] P. Castonguay, P. E. Vincent, and A. Jameson. A new class of high-order energy stable flux reconstruction schemes for triangular elements. *Journal of Scientific Computing*, 51(1):224–256, 2012.
- [8] J. Chan. On discretely entropy conservative and entropy stable discontinuous galerkin methods. *Journal of Computational Physics*, 362:346–374, 2018.
- [9] J. Chan, D. C. Fernandez, and M. H. Carpenter. Efficient entropy stable Gauss collocation methods. *arXiv preprint arXiv:1809.01178*, 2018.
- [10] T. Chen and C.-W. Shu. Entropy stable high order discontinuous galerkin methods with suitable quadrature rules for hyperbolic conservation laws. *Journal of Computational Physics*, 345:427–461, 2017.
- [11] G. Cohen, X. Ferrieres, and S. Pernet. A spatial high-order hexahedral discontinuous Galerkin method to solve Maxwell’s equations in time domain. *Journal of Computational Physics*, 217(2):340–363, 2006.
- [12] D. C. D. R. Fernández, J. E. Hicken, and D. W. Zingg. Review of summation-by-parts operators with simultaneous approximation terms for the numerical solution of partial differential equations. *Computers & Fluids*, 95:171–196, 2014.
- [13] D. Funaro. *Polynomial approximation of differential equations*, volume 8. Springer Science & Business Media, 2008.
- [14] G. J. Gassner. A skew-symmetric discontinuous Galerkin spectral element discretization and its relation to SBP-SAT finite difference methods. *SIAM Journal on Scientific Computing*, 35(3):A1233–A1253, 2013.
- [15] G. J. Gassner and D. A. Kopriva. A comparison of the dispersion and dissipation errors of Gauss and Gauss-Lobatto discontinuous Galerkin spectral element methods. *SIAM Journal on Scientific Computing*, 33(5):2560–2579, 2011.
- [16] J. Glaubitz, P. Öffner, and T. Sonar. Application of modal filtering to a spectral difference method. *Mathematics of Computation*, 87(309):175–207, 2018.
- [17] J. Hesthaven and R. Kirby. Filtering in Legendre spectral methods. *Mathematics of Computation*, 77(263):1425–1452, 2008.
- [18] J. S. Hesthaven and T. Warburton. Nodal high-order methods on unstructured grids: I. time-domain solution of maxwell’s equations. *Journal of Computational Physics*, 181(1):186–221, 2002.
- [19] F. J. Hindenlang and G. J. Gassner. On the order reduction of entropy stable dgsem for the compressible euler equations. *arXiv preprint arXiv:1901.05812*, 2019.
- [20] H. Huynh. A flux reconstruction approach to high-order schemes including discontinuous Galerkin methods. *AIAA paper*, 4079:2007, 2007.
- [21] H. Huynh, Z. J. Wang, and P. E. Vincent. High-order methods for computational fluid dynamics: A brief review of compact differential formulations on unstructured grids. *Computers & Fluids*, 98:209–220, 2014.
- [22] A. Jameson. A proof of the stability of the spectral difference method for all orders of accuracy. *Journal of Scientific Computing*, 45(1-3):348–358, 2010.

- [23] U. Koley, S. Mishra, N. H. Risebro, and M. Svärd. Higher order finite difference schemes for the magnetic induction equations. *BIT Numerical Mathematics*, 49(2):375–395, 2009.
- [24] D. A. Kopriva, J. Nordström, and G. J. Gassner. Error boundedness of discontinuous Galerkin spectral element approximations of hyperbolic problems. *Journal of Scientific Computing*, 72(1):314–330, 2017.
- [25] H.-O. Kreiss and G. Scherer. Finite element and finite difference methods for hyperbolic partial differential equations. *Mathematical aspects of finite elements in partial differential equations*, (33):195–212, 1974.
- [26] J. Manzanero, G. Rubio, E. Ferrer, E. Valero, and D. A. Kopriva. Insights on aliasing driven instabilities for advection equations with application to Gauss–Lobatto discontinuous Galerkin methods. *Journal of Scientific Computing*, 75(3):1262–1281, 2018.
- [27] J. Nordström. Error bounded schemes for time-dependent hyperbolic problems. *SIAM Journal on Scientific Computing*, 30(1):46–59, 2007.
- [28] J. Nordström. A roadmap to well posed and stable problems in computational physics. *Journal of Scientific Computing*, 71(1):365–385, 2017.
- [29] J. Nordström and R. Gustafsson. High order finite difference approximations of electromagnetic wave propagation close to material discontinuities. *Journal of Scientific Computing*, 18(2):215–234, 2003.
- [30] P. Öffner. *Zweidimensionale klassische und diskrete orthogonale Polynome und ihre Anwendung auf spektrale Methoden zur Lösung hyperbolischer Erhaltungsgleichungen*. PhD thesis, TU Braunschweig, 2015.
- [31] P. Öffner and H. Ranocha. Error boundedness of discontinuous galerkin methods with variable coefficients. *Journal of Scientific Computing*, pages 1–36, 2019.
- [32] P. Öffner and T. Sonar. Spectral convergence for orthogonal polynomials on triangles. *Numerische Mathematik*, 124(4):701–721, 2013.
- [33] H. Ranocha. Shallow water equations: Split-form, entropy stable, well-balanced, and positivity preserving numerical methods. *GEM – International Journal on Geomathematics*, 8(1):85–133, 04 2017.
- [34] H. Ranocha. Generalised summation-by-parts operators and variable coefficients. *Journal of Computational Physics*, 362:20–48, 02 2018.
- [35] H. Ranocha, P. Öffner, and T. Sonar. Summation-by-parts operators for correction procedure via reconstruction. *Journal of Computational Physics*, 311:299–328, 2016.
- [36] H. Ranocha, P. Öffner, and T. Sonar. Extended skew-symmetric form for summation-by-parts operators and varying jacobians. *Journal of Computational Physics*, 342:13–28, 2017.
- [37] M. Svärd and J. Nordström. Review of summation-by-parts schemes for initial-boundary-value problems. *Journal of Computational Physics*, 268:17–38, 2014.
- [38] P. E. Vincent, P. Castonguay, and A. Jameson. A new class of high-order energy stable flux reconstruction schemes. *Journal of Scientific Computing*, 47(1):50–72, 2011.
- [39] P. E. Vincent, A. M. Farrington, F. D. Witherden, and A. Jameson. An extended range of stable-symmetric-conservative flux reconstruction correction functions. *Computer Methods in Applied Mechanics and Engineering*, 296:248–272, 2015.
- [40] A. R. Winters and G. J. Gassner. A comparison of two entropy stable discontinuous Galerkin spectral element approximations for the shallow water equations with non-constant topography. *Journal of Computational Physics*, 301:357–376, 2015.